Generation of stable heading representations in diverse visual scenes

https://doi.org/10.1038/s41586-019-1767-1

Received: 29 December 2018

Accepted: 7 October 2019

Sung Soo Kim[1,3,4]*, Ann M. Hermundstad[1], Sandro Romani[1], L. F. Abbott[1,2] & Vivek Jayaraman[1]*

Many animals rely on an internal heading representation when navigating in varied environments[1–10]. How this representation is linked to the sensory cues that define different surroundings is unclear. In the fly brain, heading is represented by 'compass' neurons that innervate a ring-shaped structure known as the ellipsoid body[3,11,12]. Each compass neuron receives inputs from 'ring' neurons that are selective for particular visual features[13–16]; this combination provides an ideal substrate for the extraction of directional information from a visual scene. Here we combine two-photon calcium imaging and optogenetics in tethered flying flies with circuit modelling, and show how the correlated activity of compass and visual neurons drives plasticity[17–22], which flexibly transforms two-dimensional visual cues into a stable heading representation. We also describe how this plasticity enables the fly to convert a partial heading representation, established from orienting within part of a novel setting, into a complete heading representation. Our results provide mechanistic insight into the memory-related computations that are essential for flexible navigation in varied surroundings.

Internal representations of the spatial relationship of an animal to its surroundings are essential for flexible navigation[3,8–10]. Although these representations must be stable to be useful for planning and goal-oriented behaviour, they must also adapt to changes in environmental and behavioural contexts. Indeed, the representations provided by head-direction cells, grid cells and place cells are all known to remap in different surroundings on the basis of spatially relevant sensory information[23–26]. A central question in navigation concerns how the brain carries out this flexible transformation of sensory information into a stable internal representation[2,27]. In insects, a multifunctional brain region known as the central complex[11] (Fig. 1a) has a key role in visually guided navigation, including flexible heading selection[7,9,28] and place learning[29]. Many of these abilities rely on successfully incorporating visual information from landscapes[30] or the pattern of polarized light and chromatic gradients in the sky[4,5,31] to generate an internal representation of heading in the central complex; specifically, a bump of activity in compass neurons (also known as E–PG neurons; see 'Nomenclature' in Methods) in the ellipsoid body[3], a substructure of the central complex (Fig. 1a, b). These neurons are an important part of a ring attractor network[32] that maintains and updates the heading representation on the basis of self-motion[33,34] and visual signals[3]. Visual inputs are brought to the ellipsoid body by GABAergic (γ-aminobutyric-acid-releasing) ring neurons[12], which have localized spatiotemporal receptive fields[13–16] (Fig. 1c). Here we show how network plasticity enables the flexible generation of a stable compass-neuron heading representation in different visual scenes.

Remapping of heading representation

To explore the flexibility of heading representation in the fly, we used two-photon calcium imaging to monitor responses of the compass-neuron population in head-fixed flies that were flying in a virtual-reality arena, which consisted of panels of light-emitting diodes. The virtual-reality setup gave the insect one-dimensional, closed-loop control of its orientation[32] relative to visual scenes (Fig. 1d–g, Methods). Visual environments were derived from two natural scenes (Fig. 1h, i). The compass-neuron response in these scenes rapidly stabilized into an activity bump in the ellipsoid body that maintained a consistent angular relationship to the visual scene as the fly turned (Fig. 1h, i). Previous studies[3,9,10,32] in simpler visual settings (such as a single stripe) have shown that the bump tracks the visual scene, but with an offset between the angular position of the bump in the ellipsoid body and the angular orientation of the stripe relative to the fly. This pinning offset between the bump and visual cues (Methods) seldom changes across trials for a given fly in a specific visual setting, but differs across flies[3,32–34]. We found that the pinning offset also varied substantially across different naturally derived scenes for a single fly, and across flies for the same scene (Fig. 1j). We argue that this variable but stable offset is the natural outcome of plasticity in synapses that flexibly maps visual scenes onto the heading representation.

If activity-dependent plasticity between visual inputs and compass neurons underlies the observed variability in offset (Fig. 1j), experiencing an imposed artificial relationship between the scene and the bump should induce a sustained change in offset (as proposed for mammalian navigation systems[17,18]). A previous study of tethered flying flies used two-photon-localized optogenetics to temporarily displace a compass-neuron bump in the ellipsoid body by an arbitrary angle[32]. As in this previous study, here the original bump (Fig. 2a, d top) was quickly replaced by a displaced bump generated by focal optogenetics (Fig. 2b, Extended Data Fig. 1a). We then paired this artificial bump with an open-space scene (Fig. 1i) that was placed at a predetermined

---

[1]Janelia Research Campus, Howard Hughes Medical Institute, Ashburn, VA, USA. [2]Zuckerman Mind Brain Behavior Institute, Columbia University, New York, NY, USA. [3]Present address: Department of Molecular, Cellular, and Developmental Biology, University of California, Santa Barbara, Santa Barbara, CA, USA. [4]Present address: Neuroscience Research Institute, University of California, Santa Barbara, Santa Barbara, CA, USA. *e-mail: sungsoo@ucsb.edu; vivek@janelia.hhmi.org

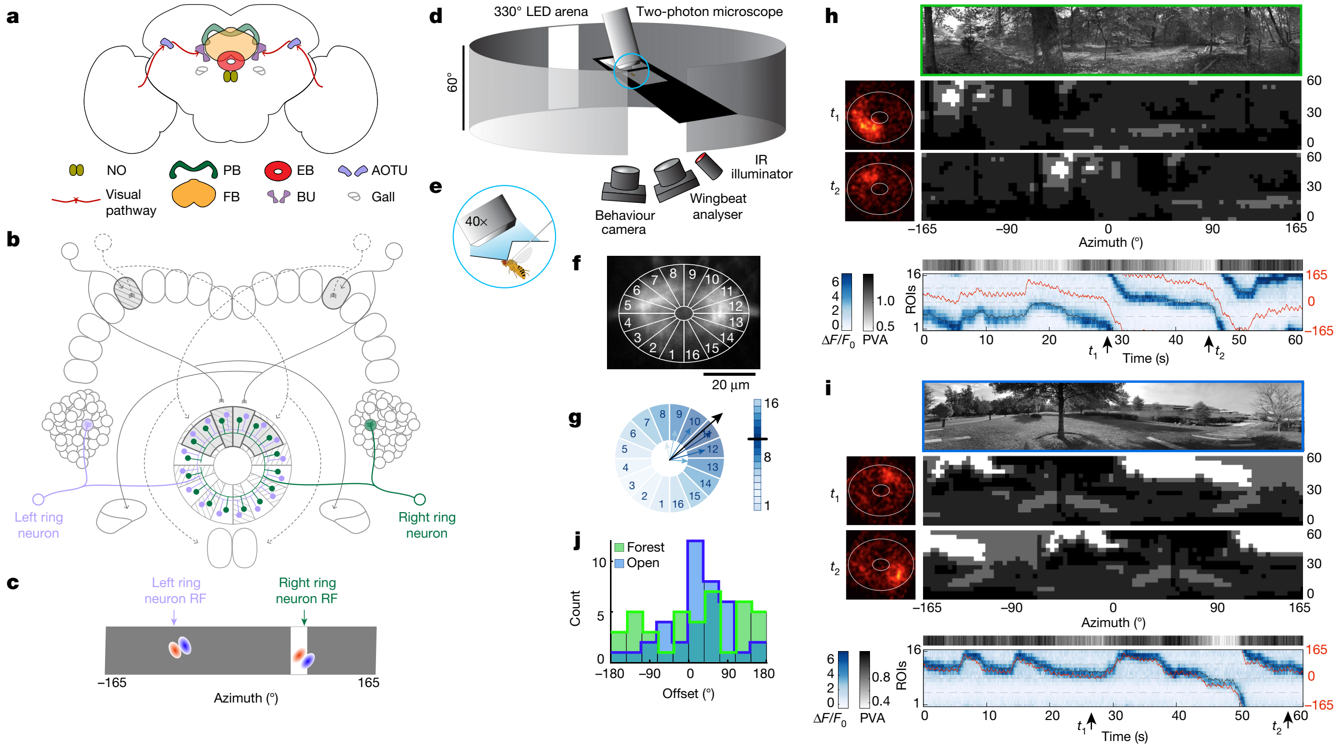

Fig. 1 | E–PG neurons stably represent heading in different visual environments. **a**, Central complex. Visual inputs to the ellipsoid body arrive from the optic lobe through the anterior optic tubercle to ring-neuron dendrites in the bulb[14,15]. EB, ellipsoid body; PB, protocerebral bridge; BU, bulb; FB, fan-shaped body; NO, noduli; AOTU, anterior optic tubercle. **b**, Ring neurons (purple and green) project from the bulb to the entire circumference of the ellipsoid body. E–PG or compass neurons (solid grey arrows) innervate single ellipsoid-body wedges. Circuit details have previously been published[33]. Dashed arrows, P–EN neurons (angular velocity). Small blobs in the ellipsoid body, synapses between ring and compass neurons. **c**, Fictive sample receptive fields (red, excitatory; blue, inhibitory) of two ring neurons (purple and green in **b**) shown in a flattened representation of the visual field (grey rectangle). The vertical stripe presented in the visual arena activates the green ring neuron. RF, receptive field. **d**, Imaging setup. IR, infrared; LED, light-emitting diode. **e**, Tethered flying fly. **f**, Ellipsoid body segmented into 16 regions of interest (ROIs). **g**, Population vector average (PVA) of $\Delta F/F_0$ computed to obtain the angular position and amplitude of the compass-neuron activity bump. **h**, Compass-neuron calcium transients during closed-loop tethered flight in a visual environment derived from a natural scene (forest; shown at the top). Middle, actual scene presented on an arena of blue light-emitting diodes with discretized brightness. Snapshots of compass-neuron activity in the ellipsoid body at times t_1 and t_2, corresponding to different scene orientations. Bottom, $\Delta F/F_0$ of 16 ROIs over time. Greyscale band, PVA amplitude. Red line, scene orientation. GCaMP signal colour-coded in blue. Black line, PVA. **i**, Calcium transients from the fly in **h** in a different scene (top), open space. **j**, Distribution of mean pinning offset across flies. Offset distribution for the open-space scene is significantly different from uniform for unknown reasons (open-space scene, 39 trials, 10 flies, unimodality test by randomization, $P < 0.0001$; forest scene, 40 trials, 10 flies, $P = 0.3603$).

angular position in the arena relative to the bump (Fig. 2b, d middle, Supplementary Video 1). We repeatedly shifted the artificial bump through eight positions around the ellipsoid body, while simultaneously shifting the scene around the visual arena to maintain its fixed angular relationship to the imposed bump (Fig. 2b, d middle). A 5-min pairing protocol was sufficient to change the offset, and the newly imposed relationship between the visual scene and the compass-neuron bump was clearly preserved in subsequent closed-loop probe trials (Fig. 2c, d bottom, Extended Data Fig. 1f, h, l). Such remapping could also be induced with simpler visual scenes (such as a single stripe; Extended Data Fig. 1b, e, g, i, m), but could not be induced without the optogenetic reagent or in darkness (Extended Data Fig. 1j, k, n, o). Thus, we find strong experimental support for plasticity that enables visual surroundings to be flexibly remapped onto the compass-neuron population upon sustained experience of a specific angular relationship between the bump and the scene.

Plasticity creates a stable compass

The experience-dependent remapping that we observed (Fig. 2a–d), which involves co-activation of specific visual inputs and compass neurons, is strongly suggestive of Hebbian plasticity, which has been hypothesized to explain how mammalian head-direction cells tether to visual cues[17,18]. We built an anatomically motivated circuit model to better understand the effect of such a plasticity mechanism on scene-to-bump remapping. The key components of the model (Fig. 2e–h; implementation details are given in the Supplementary Information) are: (i) visual ring neurons that distribute information about visual features to all compass neurons throughout the ellipsoid body[13–15,35] (Fig. 1b, c, 2f)—for simplicity, we treat ring-neuron receptive fields as encoding only azimuthal information, and address the two-dimensional spatiotemporal complexity of their responses[14] in a later section; (ii) ring attractor dynamics, a form of all-to-all competitive network dynamics that ensures a single compass-neuron bump that can remain active in darkness[32–34]; (iii) a plasticity rule through which the co-activation of GABAergic inhibitory ring neurons and compass neurons results in a depression of the synaptic weight between them[36] (inhibitory Hebbian plasticity[17–21]), whereas the activation of compass neurons alone results in potentiation (alternative plasticity rules are given in Supplementary Information). In this model (which shares some conceptual similarities with recent models of mammalian head-direction cells[20] and grid cells[22]), the turns that the fly undertakes cause a retinotopic shift of the visual stimulus (which activates a different set of ring neurons), and angular velocity signals that are carried by so-called P–EN neurons[33,34] (dotted lines in Fig. 1b) rotate the compass-neuron bump. For a stable heading representation, bump positions driven by visual input and

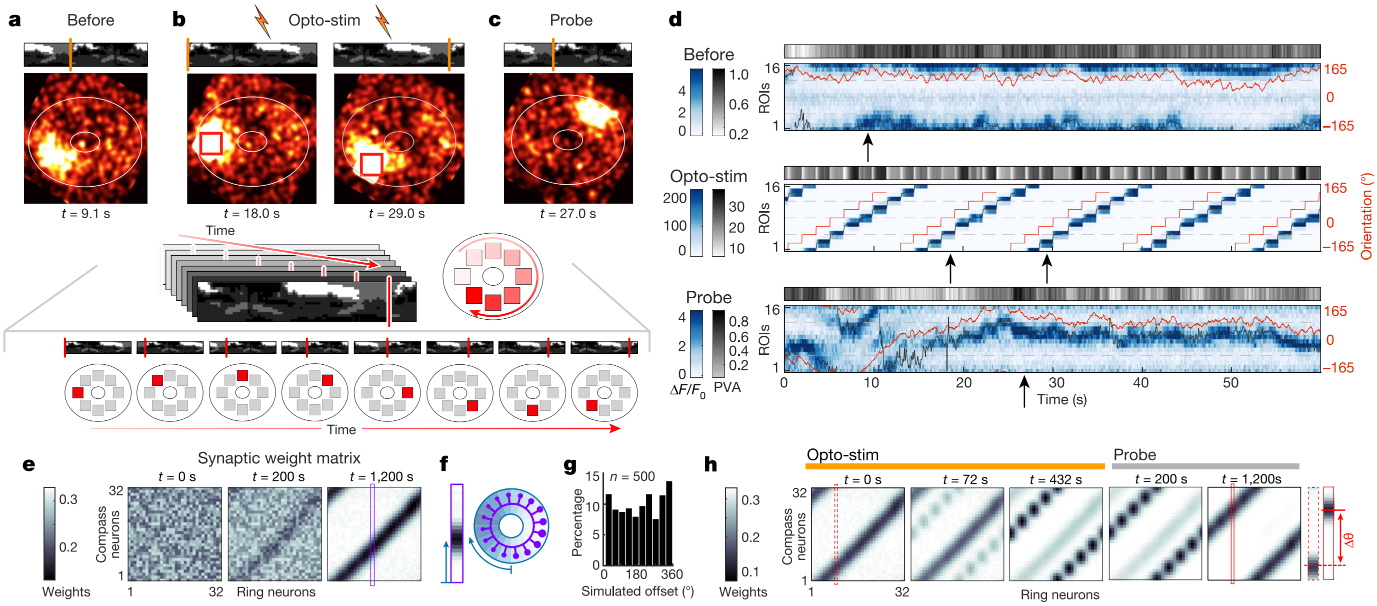

Fig. 2 | Manipulation of heading representation pinning offset. a–**d**, Activity snapshots of compass neurons before (**a**), during (**b**) and after (**c**) optogenetic manipulation in an open loop (imposed natural-scene orientations at the top, with vertical red lines emphasizing the relative orientations). Extended Data Figure 1a provides details of the optogenetic stimulation (opto-stim) protocol. **a**, Original pinning offset (arrow in **d**, top, shows the time of this snapshot). **b**, Optogenetic imposition of new offset. **b**, Top left, bump imposed on left side of the ellipsoid body (below, red rectangle) when scene oriented as at the top. **b**, Top right, 45° counter-clockwise rotated scene and bump with offset as in left. **b**, Middle, sequence of optogenetically imposed ellipsoid-body offsets (**d**, middle) (Methods). **b**, Bottom, expanded view of same sequence as shown in **b** (middle). **c**, After manipulation. The bump position relative to the same visual scene orientation as in **a**, shifted by offset imposed in **b** (compare **d**, top and bottom). **d**, Compass neuron activity before (top), during (middle) and after (bottom) optogenetic manipulation (Supplementary Video 1). Arrow in the top panel corresponds to **a**; arrows in the middle panel correspond to the left and right panels of **b** (top); and arrow in the bottom panel corresponds to **c**. **e**, Simulation snapshots. Time-varying synaptic weights between ring and compass neurons (Extended Data Fig. 2). Simulation begins with random synaptic weights (left). Synapses between coactive ring and compass neurons are weakened. Synapses from inactive ring to active compass neurons are potentiated (see Supplementary Information for different plasticity rules). The weight matrix stabilizes over time (right) (Supplementary Video 2). Vertical purple rectangle, sample mapping from ring neuron 16 to all compass neurons. **f**, Simulated compass neurons when ring neuron 16 is active. **g**, Distribution of bump offsets across 500 simulations. **h**, Simulated optogenetic bump shift. Left, weight matrix before manipulation. Second and third from the left, a new map develops while the existing map weakens. Rightmost two panels, consolidation of the new map during a probe trial. Dashed red rectangle, initial synaptic weights from ring neuron 9 to compass neurons. Solid red rectangle, same weights after consolidation; offset shifted.

angular velocity should be in register. That is, for any given heading, plasticity should ensure that inhibitory ring neurons create a position of decreased inhibition in the ellipsoid body that coincides with where the P–EN input moves the bump—essentially a self-consistent mapping of visual cues onto the bump.

We first tested the model for a simple scene with a single vertical stripe (Extended Data Fig. 1b–e), simulating the fly turning through the scene (Fig. 2e–g, Supplementary Video 2; a complex scene is shown in Extended Data Fig. 2a–c). These rotations ensured both that the bump travelled around the ellipsoid body and that ring neurons corresponding to all visual-feature positions were selectively co-activated at appropriate angular orientations. Starting with random synaptic weights, Hebbian plasticity produced a spatially consistent mapping and stable offset between the heading representation and the angular position of the single visual feature (Fig. 2e). Simulating optogenetic manipulation as a current injection into model compass neurons reproduced the remapping phenomenon (Fig. 2h, Extended Data Fig. 2d, e). These results account for the varying offsets observed across flies[3], the persistence of an offset for a given scene in a single fly and the flexibility that allows the ellipsoid body to track heading within different visual scenes.

Optogenetic inversion of the map

In further simulations, the natural concurrence between scene movement and bump position during turns could be inverted, with visual cues overriding self-motion input to drive the bump backwards (Fig. 3a, b). In optogenetic offset-induction experiments, we found that the actual network was indeed flexible enough to induce an inverted remapping in which visual input drove the bump around the ellipsoid body in the opposite direction than would be expected (Fig. 3c, d, Supplementary Video 3). In the model, the inversion was eventually corrected after prolonged ring attractor dynamics driven by self-motion (Fig. 3b rightmost panel), but the short trial duration in our physiological experiments probably limited our ability to observe such a correction in vivo. Thus, although self-motion exerts a strong influence over bump movement, network plasticity allows for a strong and notably flexible driving role for visual cues.

Remapping after experiencing ambiguity

Ring attractor dynamics ensures a single heading representation at any given time even for complex scenes, but under some circumstances this can be unstable[4]. For example, a scene with two identical stripes at diagonally opposite locations (Extended Data Fig. 3a) makes orientation within the scene inherently ambiguous[3]. Our model predicts that, upon prolonged exposure to this two-stripe scene, the plasticity mechanism creates a visual map with two potential offset angles. If a single-stripe scene is then presented, this results in two competing heading representations, with the ring attractor network selecting one of them at any particular time (Extended Data Fig. 3b, c). We found a similar effect experimentally in some probe trials after just 5 min of in vivo

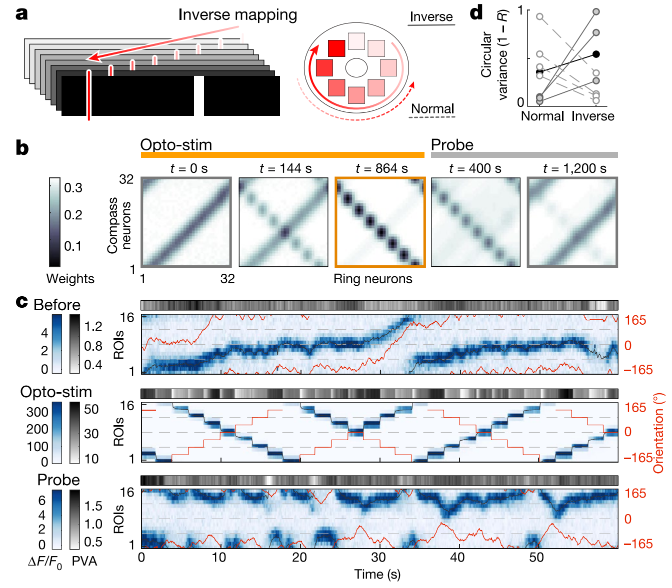

Fig. 3 | Optogenetically imposed inverse mapping of visual scene onto compass neurons. a, Inverse mapping protocol, in which the stripe is angularly displaced opposite to the optogenetic bump displacement. **b**, Simulation of inverse mapping. Inverse mapping is complete after 864 s, and maintained during initial period of probe trial (left panel under 'probe'). Sustained angular velocity input eventually corrects the map in simulations (right panel under 'probe'). **c**, Segments (60 s) of in vivo calcium transients before (top), during (middle) and after (bottom) a 10-min manipulation. Before manipulation, the bump followed the direction of stripe motion (top). After manipulation, bump motion mirrors stripe motion but in the opposite angular direction (bottom) (Supplementary Video 3). **d**, Circular variance of bump offset during the probe trial, computed for the normal arrangement of ellipsoid-body ROIs (normal), and for the inverse arrangement of ellipsoid-body ROIs (inverse). Four out of eight flies tested showed a smaller circular variance for the inverted arrangement of ellipsoid-body ROIs (white dots), indicating that the map was indeed inverted. Poor bump tracking—resulting from incomplete map manipulation—was observed in one fly, resulting in intermediate circular variances for both maps (black solid dots). Grey solid dots, three flies maintained the correct map.

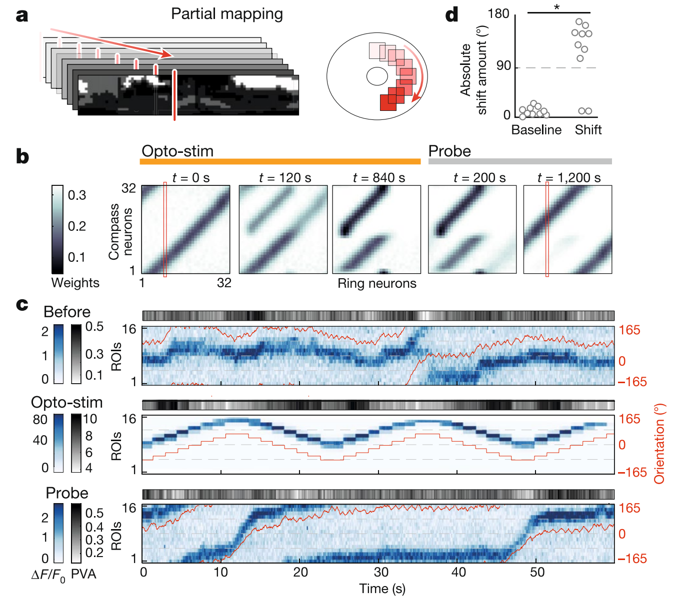

Fig. 4 | Experience of only 180° of rotation during optogenetic manipulation suffices to induce global remapping. a, Experimental protocol in which optogenetic manipulation and the experience of scene orientations span only 180°. **b**, Simulation of protocol with a simple single-stripe scene. After manipulation (t = 840 s under optogenetic stimulation), there are two sets of weak synapses (top left and bottom left), and the upper right corner of the weight matrix is completely erased. During the probe trial, a newly imposed offset propagated across the entire weight matrix (probe). **c**, Segments (60 s) of compass-population calcium transients before (top), during (middle) and after (bottom) optogenetic manipulation, spanning 180° of the ellipsoid body and using a naturalistic scene as oriented in **a**. Compare the offsets in the top and bottom panels. **d**, Distribution of absolute offset shift across flies. Left, baseline before manipulation. Right, offset shift by manipulation (10 flies, two-sided bootstrap test of mean difference, *P = 0.0002).

closed-loop experience with a two-stripe scene in the absence of any optogenetic manipulation (Extended Data Fig. 3d–i, Supplementary Video 4). A companion study[37] to this Article finds electrophysiological and imaging signatures of offset switches in a larger fraction of experiments after walking flies experience such ambiguous scenes for longer durations. These results demonstrate how exposure to an ambiguous visual scene can, through the interactive influence of plasticity and ring attractor dynamics, affect the reliability of an otherwise-stable heading representation.

Building a full map from partial views

In our remapping experiments thus far, the fly performed multiple complete rotations to establish a stable heading representation in a novel setting, which seems unlikely under natural conditions. *Drosophila* can see nearly 320° of the visual scene from a single orientation[38] and the E–PG bump typically activates more than 90° of the ellipsoid body[3]; this suggests that even limited experience of a scene should trigger Hebbian plasticity that affects a large sector of the ellipsoid body. In the model, we found that full mapping of a visual scene could occur even if the bump was rotated only by 180° or less during optogenetic manipulation (Fig. 4a, b, Extended Data Fig. 4). We directly tested this prediction by imposing an angular relationship between a vertical stripe and an artificial compass-neuron bump, but this time limiting the range of bump positions to 180°. Indeed, we found that—in the majority of flies (6 out of 10)—experiencing this limited range of bump positions was sufficient to induce a stable heading that matched the imposed offset in the probe period of the trial (Extended Data Fig. 4d, e). We could successfully induce a full remapping of the single-stripe scene in a few flies even in a more-constrained situation in which the range of bump positions spanned only 60° (in 7 out of 20 flies) (Extended Data Fig. 4i–k). Further analysis revealed that successful remapping was more likely when the stripe and the bump started inside the newly mapped region in the probe trial, consistent with simulations (Extended Data Fig. 4f–h, j, k). This probably occurred because the internally generated angular velocity signal could move the bump into regions that were not previously traversed while still preserving the new offset, thereby allowing the new heading representation to stabilize. We also observed full remapping after limited-angle exposure in experiments with a natural scene (Fig. 4a, c, d). These results provide insights into how Hebbian plasticity combined with ring attractor dynamics enables the fly to convert information gathered from limited views of a novel scene into a complete heading representation within that scene.

Stability of the compass in two-dimensional scenes

Looking across all experiments, we observed that heading representations exhibit a varying degree of stability across different scenes (Fig. 5a, b). We wondered whether structure in the vertical dimension—typical for natural scenes and known to be encoded by visual ring neurons[13,14,39]—could resolve potential ambiguities in scenes with repeating visual features in the horizontal dimension (for example,

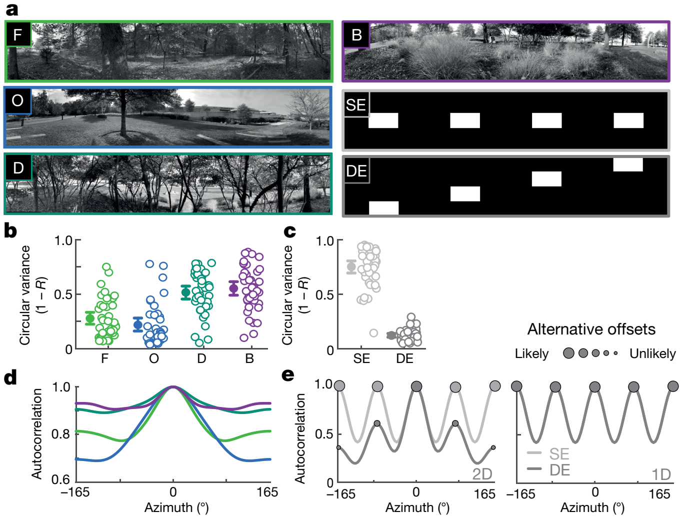

Fig. 5 | The stability of bump dynamics is predicted by two-dimensional information in visual scenes. a, Four natural scenes (F, forest (Fig. 1h); O, open field (Fig. 1i); D, dense forest; and B, bush) were downsampled and discretized. Two artificial scenes with the same local features at the same (SE) and different elevations (DE) were also used. **b**, Circular variance of instantaneous pinning offset with natural scenes (4 repetitions of 2 scenes per fly, 40 trials from 10 flies for each condition) (Methods). The bump reliably tracked the orientation of forest and open-space scenes (indicated by low circular variance). F, mean = 0.2771, 95% confidence interval = [0.2231, 0.3344]; O, mean = 0.2180, 95% confidence interval = [0.1616, 0.2828]). Tracking was poor (a high circular variance) for dense-forest and bush scenes. D, mean = 0.5163, 95% confidence interval = [0.4557, 0.5752]; B, mean = 0.5528, 95% confidence interval = [0.4893, 0.6135]). Bootstrap tests of the difference in mean circular variance between each pair of scenes showed significant difference across all pairs (two-sided, $P < 0.0001$), except between forest and open-space scenes (two-sided, $P = 0.169$) and between dense-forest and bush scenes ($P = 0.406$). **c**, Circular variance of instantaneous pinning offset for the same-elevation and different-elevation artificial scenes (4 repetitions of both scenes per fly, 40 trials from 10 flies) (Methods). The offset was stable (a low circular variance) for the different-elevation scene (mean = 0.1212, 95% confidence interval = [0.1046, 0.1392]), but not for the same-elevation scene (mean = 0.7521, 95% confidence interval = [0.6937, 0.8045]). The mean circular variance between scenes was significantly different (two-sided bootstrap test, $P < 0.0001$). **d**, Two-dimensional autocorrelation of natural scenes. **e**, One-dimensional (1D; right) and two-dimensional (2D; left) autocorrelation of the same-elevation and different-elevation artificial scenes; the one-dimensional autocorrelation is identical, but the two-dimensional autocorrelations are different.

the 'same-elevation' scene in Fig. 5a). Using artificial stimuli, we found that the bump reliably tracked the orientation of an artificial scene with four identical objects placed at different elevations, whereas it could not stably track when these objects were placed at the same elevation (Fig. 5c). This stability is well-predicted by the fact that the two-dimensional autocorrelation of each scene is distinctly single-peaked (Fig. 5d, e). We conclude that the two-dimensional organization of a scene[13,14,39] contributes to the generation and stability of the pinning offset.

Some insects are capable of snapshot-based navigation[30,31,40,41] in which stored visual scenes are recalled to drive scene-specific directional actions. Further analysis of our model indicated that multiple visual maps can be stored simultaneously if plasticity between visual ring neurons and compass neurons is presynaptically gated and the network has access to a rich ring-neuron representation of visual scenes[15,35] (Extended Data Figs. 5, 6, Supplementary Information). Other spatially informative sensory inputs—including spectral[42], mechanical (for example, wind[43]) and olfactory cues[44]—may also contribute to differentiating natural sensory environments.

Discussion

We have shown how inhibitory Hebbian plasticity can rapidly transform visual feature information into an attractor-driven internal representation. Angular velocity input to the attractor converts an emerging mapping on the basis of limited views of a scene into a complete and consistent heading representation, a potentially critical function in animal navigation. The induction of inverse maps emphasizes the notable flexibility of the system. A key issue that remains unresolved is the nature of bump dynamics during translation in a two-dimensional environment. Mammalian head-direction cells are unaffected by translation[1], but our model suggests that the compass circuit tracks the angle between the orientation of the fly and an object in the visual scene without correcting for translation—potentially making it a local compass. However, the plasticity that we have identified required only a few minutes, and may be even faster under natural conditions when the system can co-opt an existing mapping from ring to compass neurons. In our simulations (data not shown), this timescale prevented nearby objects and transient stimuli—such as neighbouring conspecifics that would not move coherently with the bearing of the fly—from being mapped, but tethered the compass to distant objects that moved coherently with the turns of the fly.

The locus of plasticity is likely to be synapses between ring and compass neurons; this idea is also favoured by the authors of the accompanying Article[37], who present electrophysiological evidence that is consistent with plasticity altering inhibitory visual inputs to individual compass neurons. At a synaptic and biophysical level, it remains to be seen how the Hebbian mechanism that we have proposed relates to, and interacts with, other forms of plasticity such as spike-timing-dependent plasticity[45,46], or with plasticity-inducing mechanisms such as nitric oxide signalling in the ellipsoid body[47], dopaminergic modulation (as seen in the fly mushroom body[36,48]) or plateau potentials (as seen during remapping of hippocampal place cells[49]).

Our results support a model in which plasticity is constantly active to allow rapid adaptation to new settings, enabling the ring attractor to generate a single heading direction even in a complex environment. Such stable sensorimotor representations probably enable animals to overcome transient uncertainties in their surroundings as they pursue diverse behavioural goals.

Online content

Any methods, additional references, Nature Research reporting summaries, source data, extended data, supplementary information, acknowledgements, peer review information; details of author contributions and competing interests; and statements of data and code availability are available at https://doi.org/10.1038/s41586-019-1767-1.

1. Taube, J. S. The head direction signal: origins and sensory-motor integration. *Annu. Rev. Neurosci.* **30**, 181–207 (2007).
2. Geva-Sagiv, M., Las, L., Yovel, Y. & Ulanovsky, N. Spatial cognition in bats and rats: from sensory acquisition to multiscale maps and navigation. *Nat. Rev. Neurosci.* **16**, 94–108 (2015).
3. Seelig, J. D. & Jayaraman, V. Neural dynamics for landmark orientation and angular path integration. *Nature* **521**, 186–191 (2015).
4. Heinze, S. & Reppert, S. M. Sun compass integration of skylight cues in migratory monarch butterflies. *Neuron* **69**, 345–358 (2011).
5. Heinze, S. & Homberg, U. Maplike representation of celestial *E*-vector orientations in the brain of an insect. *Science* **315**, 995–997 (2007).
6. Varga, A. G. & Ritzmann, R. E. Cellular basis of head direction and contextual cues in the insect brain. *Curr. Biol.* **26**, 1816–1828 (2016).
7. el Jundi, B. et al. Neural coding underlying the cue preference for celestial orientation. *Proc. Natl Acad. Sci. USA* **112**, 11395–11400 (2015).
8. Butler, W. N., Smith, K. S., van der Meer, M. A. A. & Taube, J. S. The head-direction signal plays a functional role as a neural compass during navigation. *Curr. Biol.* **27**, 1259–1267 (2017).
9. Giraldo, Y. M. et al. Sun navigation requires compass neurons in *Drosophila*. *Curr. Biol.* **28**, 2845–2852 (2018).

10. Green, J., Vijayan, V., Mussells Pires, P., Adachi, A. & Maimon, G. A neural heading estimate is compared with an internal goal to guide oriented navigation. *Nat. Neurosci*. **22**, 1460–1468 (2019).
11. Turner-Evans, D. B. & Jayaraman, V. The insect central complex. *Curr. Biol*. **26**, R453–R457 (2016).
12. Hanesch, U., Fischbach, K. F. & Heisenberg, M. Neuronal architecture of the central complex in *Drosophila melanogaster*. *Cell Tissue Res*. **257**, 343–366 (1989).
13. Seelig, J. D. & Jayaraman, V. Feature detection and orientation tuning in the *Drosophila* central complex. *Nature* **503**, 262–266 (2013).
14. Sun, Y. et al. Neural signatures of dynamic stimulus selection in *Drosophila*. *Nat. Neurosci*. **20**, 1104–1113 (2017).
15. Omoto, J. J. et al. Visual input to the *Drosophila* central complex by developmentally and functionally distinct neuronal populations. *Curr. Biol*. **27**, 1098–1110 (2017).
16. Shiozaki, H. M. & Kazama, H. Parallel encoding of recent visual experience and self-motion during navigation in *Drosophila*. *Nat. Neurosci*. **20**, 1395–1403 (2017).
17. Skaggs, W. E., Knierim, J. J., Kudrimoti, H. S. & McNaughton, B. L. A model of the neural basis of the rat's sense of direction. *Adv. Neural Inf. Process. Syst*. **7**, 173–180 (1995).
18. Knierim, J. J. in *Head Direction Cells and the Neural Mechanisms of Spatial Orientation* (eds Wiener S. I. & Taube J. S.) 163–185 (MIT Press, 2005).
19. Cope, A. J., Sabo, C., Vasilaki, E., Barron, A. B. & Marshall, J. A. A computational model of the integration of landmarks and motion in the insect central complex. *PLoS ONE* **12**, e0172325 (2017).
20. Page, H. J. I. & Jeffery, K. J. Landmark-based updating of the head direction system by retrosplenial cortex: a computational model. *Front. Cell. Neurosci*. **12**, 191 (2018).
21. Campbell, M. G. et al. Principles governing the integration of landmark and self-motion cues in entorhinal cortical codes for navigation. *Nat. Neurosci*. **21**, 1096–1106 (2018).
22. Ocko, S. A., Hardcastle, K., Giocomo, L. M. & Ganguli, S. Emergent elasticity in the neural code for space. *Proc. Natl Acad. Sci. USA* **115**, E11798–E11806 (2018).
23. Knierim, J. J., Kudrimoti, H. S. & McNaughton, B. L. Interactions between idiothetic cues and external landmarks in the control of place cells and head direction cells. *J. Neurophysiol*. **80**, 425–446 (1998).
24. Fyhn, M., Hafting, T., Treves, A., Moser, M. B. & Moser, E. I. Hippocampal remapping and grid realignment in entorhinal cortex. *Nature* **446**, 190–194 (2007).
25. Solstad, T., Boccara, C. N., Kropff, E., Moser, M. B. & Moser, E. I. Representation of geometric borders in the entorhinal cortex. *Science* **322**, 1865–1868 (2008).
26. Krupic, J., Bauza, M., Burton, S., Barry, C. & O'Keefe, J. Grid cell symmetry is shaped by environmental geometry. *Nature* **518**, 232–235 (2015).
27. Connor, C. E. & Knierim, J. J. Integration of objects and space in perception and memory. *Nat. Neurosci*. **20**, 1493–1503 (2017).
28. Neuser, K., Triphan, T., Mronz, M., Poeck, B. & Strauss, R. Analysis of a spatial orientation memory in *Drosophila*. *Nature* **453**, 1244–1247 (2008).
29. Ofstad, T. A., Zuker, C. S. & Reiser, M. B. Visual place learning in *Drosophila melanogaster*. *Nature* **474**, 204–207 (2011).
30. Collett, T. S. & Zeil, J. Insect learning flights and walks. *Curr. Biol*. **28**, R984–R988 (2018).
31. el Jundi, B. et al. A snapshot-based mechanism for celestial orientation. *Curr. Biol*. **26**, 1456–1462 (2016).
32. Kim, S. S., Rouault, H., Druckmann, S. & Jayaraman, V. Ring attractor dynamics in the *Drosophila* central brain. *Science* **356**, 849–853 (2017).
33. Turner-Evans, D. et al. Angular velocity integration in a fly heading circuit. *eLife* **6**, e23496 (2017).
34. Green, J. et al. A neural circuit architecture for angular integration in *Drosophila*. *Nature* **546**, 101–106 (2017).
35. Omoto, J. J. et al. Neuronal constituents and putative interactions within the *Drosophila* ellipsoid body neuropil. **12**, 103 (2018).
36. Hattori, D. et al. Representations of novelty and familiarity in a mushroom body compartment. *Cell* **169**, 956–969 (2017).
37. Fisher, Y. E., Lu, J., D'Alessandro, I. & Wilson, R. I. Sensorimotor experience remaps visual input to a heading-direction network. *Nature* https://doi.org/10.1038/s41586-019-1772-4 (2019).
38. Buchner, E. *Dunkelanregung des Stationaeren Flugs der Fruchtfliege Drosophila*. Dipl. thesis, Univ. Tübingen (1971).
39. Dewar, A. D. M., Wystrach, A., Philippides, A. & Graham, P. Neural coding in the visual system of *Drosophila melanogaster*: how do small neural populations support visually guided behaviours? *PLOS Comput. Biol*. **13**, e1005735 (2017).
40. Judd, S. P. D. & Collett, T. S. Multiple stored views and landmark guidance in ants. *Nature* **392**, 710–714 (1998).
41. Narendra, A., Gourmaud, S. & Zeil, J. Mapping the navigational knowledge of individually foraging ants, *Myrmecia croslandi*. *Proc. R. Soc. Lond. B* **280**, 20130683 (2013).
42. Longden, K. D. Colour vision: a fresh view of lateral inhibition in *Drosophila*. *Curr. Biol*. **28**, R308–R311 (2018).
43. Suver, M. P. et al. Encoding of wind direction by central neurons in *Drosophila*. *Neuron* **102**, 828–842 (2019).
44. Jacob, P. Y. et al. An independent, landmark-dominated head-direction signal in dysgranular retrosplenial cortex. *Nat. Neurosci*. **20**, 173–175 (2017).
45. Song, S., Miller, K. D. & Abbott, L. F. Competitive Hebbian learning through spike-timing-dependent synaptic plasticity. *Nat. Neurosci*. **3**, 919–926 (2000).
46. Cassenaer, S. & Laurent, G. Hebbian STDP in mushroom bodies facilitates the synchronous flow of olfactory information in locusts. *Nature* **448**, 709–713 (2007).
47. Kuntz, S., Poeck, B. & Strauss, R. Visual working memory requires permissive and instructive NO/cGMP signaling at presynapses in the *Drosophila* central brain. *Curr. Biol*. **27**, 613–623 (2017).
48. Aso, Y. & Rubin, G. M. Dopaminergic neurons write and update memories with cell-type-specific rules. *eLife* **5**, e16135 (2016).
49. Bittner, K. C. et al. Conjunctive input processing drives feature selectivity in hippocampal CA1 neurons. *Nat. Neurosci*. **18**, 1133–1142 (2015).

Methods

No statistical methods were used to predetermine sample size. The experiments were not randomized and investigators were not blinded to allocation during experiments and outcome assessment.

Nomenclature

We follow an abbreviation convention that is agreed upon by most research groups working on the central complex[50]. For E–PG or compass neurons[32], E (ellipsoid body) before a '–' represents predominantly spiny and putatively postsynaptic processes, and P (protocerebral bridge) and G (gall) after a '–' represent predominantly bouton-like and probable presynaptic processes. When fully expanded, the abbreviation E–PG stands for $\mathrm{PB}_{\mathrm{G1-8}}$.b-EBw.s-D/Vgall.b[50]. Similarly, P–EN neurons (Fig. 1), which arborize in the noduli (N), refer to $\mathrm{PB}_{\mathrm{G2-9}}$.s-EBt.b-NO1.b neurons[50].

Terminology

In the manuscript, we use the term heading representation to describe what it is that the E–PG neurons encode. However, the representation often persists when a tethered fly is standing still on a ball[3]—that is, when it has no heading in a strict sense. On the basis of such data, we would define heading as the angular orientation of the body axis of the fly in a visual scene. Future experiments may well determine that E–PG neurons represent the head direction of the fly, but all E–PG imaging experiments thus far—including those in this study—have been performed on head-fixed flies in tethered preparations, leaving this issue unresolved.

Fly stocks

Fly stocks have previously been described[32,33]. In brief, flies with either a codon-optimized UAS-GCaMP6f[51] or a recombinant of UAS-CsChrimson-mCherry-tag[52] and UAS-GCaMP6f or codon-optimized UAS-GCaMP6f[51] were driven by split-GAL4[53,54] SS00096 from the Rubin laboratory. All experiments were performed with 6–10-day-old female flies. Flies were randomly picked from their housing vials for all experiments. All flies were raised from the egg stage on standard cornmeal and soybean-based medium[55] or with additional 0.2 mM all-*trans*-retinal[52] for flies with CsChrimson.

Fly preparation for imaging during head-fixed flight

The procedure for fly preparation has previously been described[32]. In brief, flies were anaesthetized on a cold plate at 4 °C. The front legs were removed and the proboscis was pressed into its head capsule and immobilized with wax to minimize brain movement. The fly was tethered at the tip of a tungsten wire and positioned under a custom-designed stainless-steel shim, as previously described[13,56,57]. The back of the head capsule was kept nearly vertical to maximize exposure of the eyes of the fly to the surrounding light-emitting-diode (LED) arena. UV-curable adhesive was used to fix the head under the shim, then the cuticle at the top of the head and fat cells were carefully removed and trachea were carefully pushed to the back of the brain to optically reveal the central brain.

Visual stimulation

Visual arena. The hardware has been described[32]. In brief, a female fly was placed at the centre of the arena and visual stimuli were presented on a vertically placed cylindrical LED display[58] spanning 330° in azimuth and 60° in elevation. The display was covered with multiple layers of colour filter to avoid excessive leak into a photon detector and a diffuser to avoid reflection[3,13,56]. The wingbeat amplitude of each wing was computed online by analysing images acquired with a camera, using custom-built image analysis software written in MATLAB, similar to a previously described method[57]. The image acquisition rate of the camera was 119.2 Hz, which was slow enough to capture the full shadow of wings to compute the wingbeat amplitude. For closed-loop experiments, the gain was 5.1° per second for each degree of the difference between the left and right wingbeat amplitudes (ΔWBA)[59]. Air was manually puffed at the fly if it stopped flying. The data during this stalled period were excluded from analyses.

Stimuli. We used various visual stimuli. Natural scenes were derived from panoramic photographs taken at the Janelia Research Campus. Using the full luminance resolution of the arena resulted in excessive leak into a photon detector even after multiple layers of filters, making it impossible to detect bump position (especially with extremely low laser power used for simultaneous imaging and optogenetic stimulation). Further, the level of light at full luminance was enough to activate CsChrimson in most flies. To reduce the light leak and undesired activation of CsChrimson, we downsampled and monochromatized natural scene photographs (Fig. 1h, i, 4a, 5a) to four luminance levels close to a log scale (0, 2, 6 and 15). Other visual stimuli included a bright vertical stripe spanning 60° in elevation and 15° in azimuth (Fig. 3a, Extended Data Figs. 1b, 3b, 4d, i), two bright vertical stripes 165° apart (Extended Data Fig. 3a), a random dot pattern of which each pixel is either of maximum brightness or dark, and patterns containing four small horizontal bars each spanning 30° in azimuth and 15° in elevation (Extended Data Fig. 5a, b). All the stimuli used in this study were presented on a blue LED arena. We used a greyscale in the figures for visual clarity. To avoid a sudden luminance change that might induce a startle response in flies, the 30° arena gap behind the fly was stitched in all protocols to maintain overall luminance. Thus, when an object crosses the gap, it does not disappear but jumps across it.

Protocols

Optogenetic bump offset shift. An experiment (14 flies) (Extended Data Fig. 1b–d, i, m) began with a 1-min exposure to a closed-loop random dot stimulus (trial 1). It was followed by 3 1-min closed-loop single-stripe trials (trials 2–4), a 5-min optogenetic manipulation trial that imposes a fixed 90° offset between the bump and a scene (trial 5), 3 1-min closed-loop single-stripe trials (trials 6–8), another 5-min optogenetic trial with −90° offset (trial 9), and 2 1-min closed-loop single-stripe trials (trials 10 and 11). Each trial was followed by a 15-s dark trial before the next trial started. During optogenetic manipulation trials, 8 positions in the ellipsoid body, separated by 45° (with a visual stimulus of a corresponding offset), were sequentially stimulated, each of which took approximately 2–2.5 s. The initial position of the visual stimulus during closed-loop trials was random. Trial 2 was used for flies to establish a stable offset. Trials 3 and 4 and trials 7 and 8 were used to measure the baseline variability of the bump offset within a single fly before optogenetic manipulation. Trials 6 and 7 and trials 10 and 11 were used to measure the baseline variability after optogenetic manipulation. Trials 4 and 6 were used to measure the effect of optogenetic manipulation in trial 5 (90° offset). Trials 8 and 10 were used to measure the effect of optogenetic manipulation in trial 9 (−90° offset). Control experiments (ten flies each) used the same order of trials except that either CsChrimson was not expressed (Extended Data Fig. 1j, n) or the stripe was not presented (Extended Data Fig. 1k, o) during manipulation trials. A natural scene was also tested (Fig. 2a–d, Extended Data Fig. 1f, h, l). To increase statistical power, all data collected before or after the −90° protocol were rotated 180° and pooled with the 90° protocol during analyses.

Bump offset shift with two vertical stripes. The order of trials was identical to optogenetic bump offset shift experiments, but—during manipulation trials—two stripes at opposite sides of the visual field (165° apart in the 330° arena) were presented under closed-loop control (Extended Data Fig. 3d–i). Trials 6 and 10 were used to measure the number of bumps and the bump offset variance for the initial 15 s after manipulation trials, and trials 7 and 11 were used as control trials. Ten flies were tested.

Forced optogenetic inverse mapping. There were two 1-min single-stripe closed-loop trials followed by 10 min of an optogenetic inverse mapping trial and 2 min of a probe trial (Fig. 3). Consecutive trials were separated by a 3-s dark trial.

Natural scene protocols. Two 2-min closed-loop trials with a down-sampled and monochromatized forest scene were presented (trials 1 and 2). They were followed by 2 2-min closed-loop trials with an open-space scene (trials 3 and 4), and all 4 trials were repeated (trials 5–8). All consecutive trials were separated by a 5-s dark trial. The initial scene orientation of each trial was random. Trials 2 and 5 were used to measure the offset shift between two forest-scene trials separated by open-space scene trials. Trials 4 and 7 were used to measure the offset shift between two open-space scene trials separated by forest-scene trials. Trials 2 and 3 were used to measure the offset shift during the transition from a forest scene to an open-space scene. Trials 4 and 5 were used to measure the offset shift during the transition from an open-space scene to a forest scene. Ten flies were tested (Fig. 1h, i, 5b, d). The whole protocol was repeated for another pair of less-reliable natural scenes (dense forest and bush) (Fig. 5a, b, d). Finally, to address the relevance of two-dimensional organization of the visual scene to the bump position computation, the same protocol was repeated with 2 scenes of 4 artificial objects: in each scene, four horizontal objects were presented with equal azimuthal separation and either the same or different elevations (Fig. 5a, c, e).

Bump offset shift with limited optogenetic manipulation. An experiment (Fig. 4, Extended Data Fig. 4) began with a 1-min closed-loop trial with a single stripe (trial 1). It was followed by a 2-min closed-loop single-stripe trial (trial 2), a 30-s open-loop probe trial (trial 3), a 5-min open-loop manipulation trial (trial 4), a 30-s open-loop probe trial (trial 5), a 2-min closed-loop trial (trial 6), a 30-s open-loop probe trial (trial 7), a 5-min open-loop manipulation trial (trial 8), a 30-s open-loop probe trial (trial 9) and a 2-min closed-loop trial (trial 10). All consecutive trials (except the probe trials following manipulation trials) were separated by a 3-s dark trial. The initial scene orientation of closed-loop trials was random. During trial 2, the bump offset was roughly determined by visual inspection. Then, a target offset was determined to be 180° away from this baseline offset and optogenetically imposed during manipulation trials. Three manipulation protocols were used (ten flies each). The first protocol (local protocol 1) spanned 60° of the ellipsoid body, in which 3 positions separated by 30° were optogenetically stimulated. Each position was stimulated for 1.5–2.5 s in sequence. The probe trials were composed of the same visual stimuli used during optogenetics trials to measure the effectiveness of the optogenetic manipulation. The position of a stripe in closed-loop probe trials began at the middle of the range of stripe positions used during manipulation. The second protocol (local protocol 2) spanned 60° of the ellipsoid body, in which three positions separated by 30° were optogenetically stimulated. Each position was stimulated for 1.5–2.5 s in sequence. During probe trials, two stripe positions (one at the centre of the manipulated area and another 180° away from it) were repeatedly presented (each for 3 s) to probe the global effect of local manipulations. The position of a stripe in closed-loop probe trials was random. For further analysis, flies from the two protocols (local protocols 1 and 2) were pooled (Extended Data Fig. 4j, k) and regrouped depending on the position of the bump and the stripe at the beginning of the probe trial. The final protocol (local protocol 3) spanned 180° of the ellipsoid body (Extended Data Fig. 4d), in which 8 positions separated by 22.5° were optogenetically stimulated. The same probe stimuli as in local protocol 2 were used in addition to 8 stripe positions separated by 45° to cover all orientations. The offset during probe trials was measured over the final 5 s. The final protocol was repeated with a natural scene (Fig. 4).

The position of the pattern, wingbeat amplitudes, air-puffing signal and two-photon frame trigger were all simultaneously collected using custom software written in MATLAB that used National Instrument data acquisition hardware.

Two-photon calcium imaging

Calcium imaging was performed using a custom-built two-photon microscope[60]. We used a 40× objective (NA 1.0, 2.8 mm WD) and a GaAsP photomultiplier tube (PMT). A Chameleon Ultra II laser tuned to 930 nm with a custom-built pulse compressor was used as the excitation source with a maximum power of 8 mW at the sample. We used the same saline as in previous studies[3] with adjusted calcium concentration at 2.0 mM. We imaged the ellipsoid body over 6-plane volumes using a fast remote focusing technique[61], which was modified in-house, at a rate of 9.8 Hz volume rate (256 × 256 resolution, 58.8-Hz frame rate) with an equal spacing of 3–6 μm between individual scanning planes. The objective was tilted by 30° to enable imaging of the ellipsoid body with the head of the fly at a natural, vertical angle.

Two-photon optogenetic stimulation

The protocol used was largely along previously described lines[32], but differed in a few details. A single two-photon laser source was used for both imaging and optogenetic stimulation, by temporally modulating the laser power, which was implemented using the PowerBox feature in ScanImage[60] replacing the custom MATLAB software described in previous work[32] (Extended Data Fig. 1a). Increased two-photon efficiency owing to a pulse compressor allowed a lower laser power for imaging and optogenetic stimulation than previously described[32]. For the calcium-imaging-only period, a maximum laser power of 2 mW was used for both forward and backward scanning phases. During optogenetic stimulation of CsChrimson, the laser power was kept the same except for the defined stimulation area only during the forward scanning phase, in which a maximum laser power of 30 mW (typically 20 mW) was used. To prevent tissue damage, this laser power was manually adjusted during each trial to a minimal power that was sufficient to develop a bump at the site of stimulation. On average, the optogenetically induced GCaMP signal measured during the backward scanning phase was 13.3% greater than the normal condition across flies (one-tailed paired *t*-test, $P = 0.022$) in the optogenetic bump-shifting experiment with a natural scene. This higher-than-natural activity was required to inhibit the naturally generated bump. However, two vertical-stripe protocol results indicate that plasticity can be induced at the natural activity level.

Data analysis

We used MATLAB for data analysis. To avoid bias, no statistical methods were used to predetermine the power and the sample size. The fixed-offset optogenetic experiment used 14 flies, and the forced optogenetic inverse mapping experiments relied on 8 flies. All other experiments were performed until data from 10 flies were collected.

Calculation of fluorescence changes. The background noise level was predetermined by measuring the oscillatory noise from the PMT. This level was then subtracted from all imaging data, and the data were half-rectified before further analysis. A running average intensity projection of a volume (six planes) at a given time was computed for each pixel. Then, 16 ROIs were manually assigned, as previously described[32]. Next, time series for each ROI were obtained by taking the average of the fluorescence signal within the ROI at each point in time. For calcium imaging experiments without optogenetics, $\Delta F/F_0$ was computed using F_0 as the mean of the lowest 10% of signals in each ROI. No further temporal smoothing was applied.

PVA of a bump and its amplitude. As a simple measure of the bump position and strength, the PVA was computed as the weighted vector average across ellipsoid-body wedges, with the weight determined by the fluorescence level ($\Delta F/F_0$), and the vector determined by the position of each ROI in the ellipsoid body. The amplitude of the PVA was determined as the length of the average vector. We used brewermap (S. Cobeldick, MathWorks file exchange) with a colour scheme 'blue' from http://colorbrewer2.org/ to depict all PVA plots.

Calculation of the number of bumps. For each frame, a bump was defined as any contiguous set of ROIs with $\Delta F/F_0$ greater than a threshold value (defined in each frame to be the mean $\Delta F/F_0$ across ROIs + 1 s.d.)[3] (Extended Data Fig. 3h).

Offset between the estimated bump position and the pattern position, and offset deviation. For a given trial, the first 15 s were discarded, as were time points when the fly did not fly, which were determined by the wingbeat amplitude. The offset between the absolute scene orientation (to the experimenter) and the PVA estimate was calculated as the mean angular difference for the remaining time. The deviation was calculated as the circular variance. The visual arena (covering 330°) was mapped to 360°, as was the position of the scene.

Analysis of optogenetic offset manipulation trials. The exact artificial offset imposed by optogenetic stimulation during manipulation trials was determined by the mean angular difference between the scene orientation and the PVA during optogenetic stimulation.

Circular linearity test. For the optogenetic manipulation protocol, the expected amount of offset shift was assumed to be the same as the artificially imposed amount of shift. The sum of absolute angular difference between these two values across flies was used as a test statistic. To obtain the null distribution, the observed amounts of shift were randomized across flies and the sum of absolute angular differences was calculated, all of which was repeated 10,000 times. The P value was calculated by counting the number of outcomes from randomization that were smaller than the test statistic (Extended Data Fig. 1h–k).

Circular unimodality or circular asymmetricity test. We used this test to determine whether a set of directional data was significantly unimodal or asymmetric. The circular variance of the data was used as a test statistic. Each data point was assigned a random direction sampled from a circularly uniform distribution, after which the circular variance was calculated. This random assignment procedure was repeated 10,000 times to generate a null distribution. The P value was determined by the number of times at which the circular variance was smaller than the test statistic (Fig. 1j, Extended Data Fig. 5c). This method reliably works only for unimodal data and may generate false-negative results for multimodal data.

Bootstrap test of the mean difference. This test was used to establish the difference of means of two datasets when they did not satisfy the assumption of Gaussian distributions. The difference of means of two datasets was used as a test statistic. Two sets of data were pooled, random samples were assigned to each group either with (bootstrap) or without (randomization) replacement, and the difference of the means of the two groups were calculated. This process was repeated 10,000 times to generate the null distribution. The P value was computed by counting the number of events with an outcome that was greater than the test statistic (Extended Data Fig. 1l–o). Random sampling both with and without replacement generated similar P values in all tests in our study.

Circular variance of pinning offset. The variance in pinning offset relative to each scene (Fig. 5b, c) was computed as the circular variance of the instantaneous pinning offset along the time of a single trial. Each fly experienced four repetitions of two scenes. For each scene, all trials were pooled across flies (in total, 40 trials each).

Circular variance of inverse map. The circular variance of the bump offset during the probe trial was calculated for both normally arranged ellipsoid-body ROIs and inversely arranged ellipsoid-body ROIs. If the circular variance of the latter was smaller than the former, the mapping from the visual scene orientation to compass neurons was determined to be inverted (Fig. 3d).

Binomial exact test. For Extended Data Fig. 4j, the baseline probability of flies shifting their offsets by more than 90° is 1 out of 7 if the stripe starts outside manipulated positions (red dots). Assuming binomial sampling from this distribution, the chance of 6 or more flies out of 13 shifting their offsets by more than 90° (blue dots) is $P = 0.0059$. For Extended Data Fig. 4k, the baseline probability of flies shifting their offsets by more than 90° is 3 out of 16 if the stripe or bump starts outside the manipulated positions (red dots). The chance of all 4 flies shifting their offsets by more than 90° (blue dots) assuming binomial sampling with a probability of 3/16 is $P = 0.0012$.

Natural scene analysis. Each scene was smoothed with a two-dimensional Gaussian filter with a s.d. of 4 pixels (Extended Data Fig. 5e). Then, the two-dimensional autocorrelation of each scene was calculated (Fig. 5d). Each scene was tiled horizontally (three copies) and the top and the bottom were padded with zeros. Then, MATLAB function xcorr2 was applied to this tiled scene, and to another scene representing the centre of this tiled scene. The middle range of azimuth values of the outcome (corresponding to the azimuthal range of one scene within the tiled image) was finally normalized by the maximum value to obtain two-dimensional autocorrelation. The one-dimensional autocorrelation was obtained by first taking the average intensity of the smoothed scene over elevation, then applying xcorr between this one-dimensional trace and a concatenated version of this trace, and finally normalizing by the maximum value. The two-dimensional cross-correlation was computed in the same way, except that xcorr2 was applied to two tiled scenes: one scene with three horizontal copies of itself padded at the top and bottom, and another scene without horizontal copies but padded at the top and bottom.

Reporting summary

Further information on research design is available in the Nature Research Reporting Summary linked to this paper.

Data availability

All data are freely available at http://research.janelia.org/jayaraman/Kim_etal_Nature2019_Downloads/.

Code availability

All code is freely available at http://research.janelia.org/jayaraman/Kim_etal_Nature2019_Downloads/.

50. Wolff, T. & Rubin, G. M. Neuroarchitecture of the *Drosophila* central complex: a catalog of nodulus and asymmetrical body neurons and a revision of the protocerebral bridge catalog. *J. Comp. Neurol.* **526**, 2585–2611 (2018).
51. Chen, T. W. et al. Ultrasensitive fluorescent proteins for imaging neuronal activity. *Nature* **499**, 295–300 (2013).
52. Klapoetke, N. C. et al. Independent optical excitation of distinct neural populations. *Nat. Methods* **11**, 338–346 (2014).
53. Luan, H., Peabody, N. C., Vinson, C. R. & White, B. H. Refined spatial manipulation of neuronal function by combinatorial restriction of transgene expression. *Neuron* **52**, 425–436 (2006).
54. Pfeiffer, B. D. et al. Refinement of tools for targeted gene expression in *Drosophila*. *Genetics* **186**, 735–755 (2010).
55. Guo, A. et al. Conditioned visual flight orientation in *Drosophila*: dependence on age, practice, and diet. *Learn. Mem.* **3**, 49–59 (1996).
56. Seelig, J. D. et al. Two-photon calcium imaging from head-fixed *Drosophila* during optomotor walking behavior. *Nat. Methods* **7**, 535–540 (2010).
57. Maimon, G., Straw, A. D. & Dickinson, M. H. Active flight increases the gain of visual motion processing in *Drosophila*. *Nat. Neurosci.* **13**, 393–399 (2010).

58. Reiser, M. B. & Dickinson, M. H. A modular display system for insect behavioral neuroscience. *J. Neurosci. Methods* **167**, 127–139 (2008).
59. Bahl, A., Ammer, G., Schilling, T. & Borst, A. Object tracking in motion-blind flies. *Nat. Neurosci*. **16**, 730–738 (2013).
60. Pologruto, T. A., Sabatini, B. L. & Svoboda, K. ScanImage: flexible software for operating laser scanning microscopes. *Biomed. Eng. Online* **2**, 13 (2003).
61. Rupprecht, P., Prendergast, A., Wyart, C. & Friedrich, R. W. Remote *z*-scanning with a macroscopic voice coil motor for fast 3D multiphoton laser scanning microscopy. *Biomed. Opt. Express* **7**, 1656–1671 (2016).

Acknowledgements We thank A. Jenett, T. Wolff and G. Rubin for sharing the split line SS00096; B. Pfeiffer, A. Wong, D. Anderson and G. Rubin for sharing codon-optimized GCaMP6f DNA; C. Dan for codon-optimized GCaMP6f flies; Janelia Fly Core and, in particular K. Hibbard and S. Coffman, for fly husbandry; J. Liu for virtual-reality support; V. Goncharov and C. McRaven for microscope support; J. Arnold for fly holder design; Vidrio for ScanImage support; T. Kawase for animation; and E. Nielson and S. Houck for operational support. We are grateful to A. Karpova and members of V.J.'s and A.M.H.'s laboratories for useful discussions and comments on the manuscript. S.S.K., A.M.H., S.R. and V.J. are supported by Howard Hughes Medical Institute; L.F.A. is supported by NSF NeuroNex Award DBI-1707398, the Gatsby Charitable Foundation and the Simons Collaboration for the Global Brain.

Author contributions S.S.K., A.M.H., L.F.A. and V.J. conceptualized the project; S.S.K. undertook all experiments; S.S.K. performed modelling, in collaboration with L.F.A., A.M.H. and S.R.; S.S.K., A.M.H. and V.J. provided the visualizations; S.S.K. and V.J. wrote the initial draft, and all authors contributed to editing.

Competing interests The authors declare no competing interests.

Additional information

Supplementary information is available for this paper at https://doi.org/10.1038/s41586-019-1767-1.

Correspondence and requests for materials should be addressed to S.S.K. or V.J.

Peer review information *Nature* thanks Holger G. Krapp and the other, anonymous, reviewer(s) for their contribution to the peer review of this work.

Reprints and permissions information is available at http://www.nature.com/reprints.

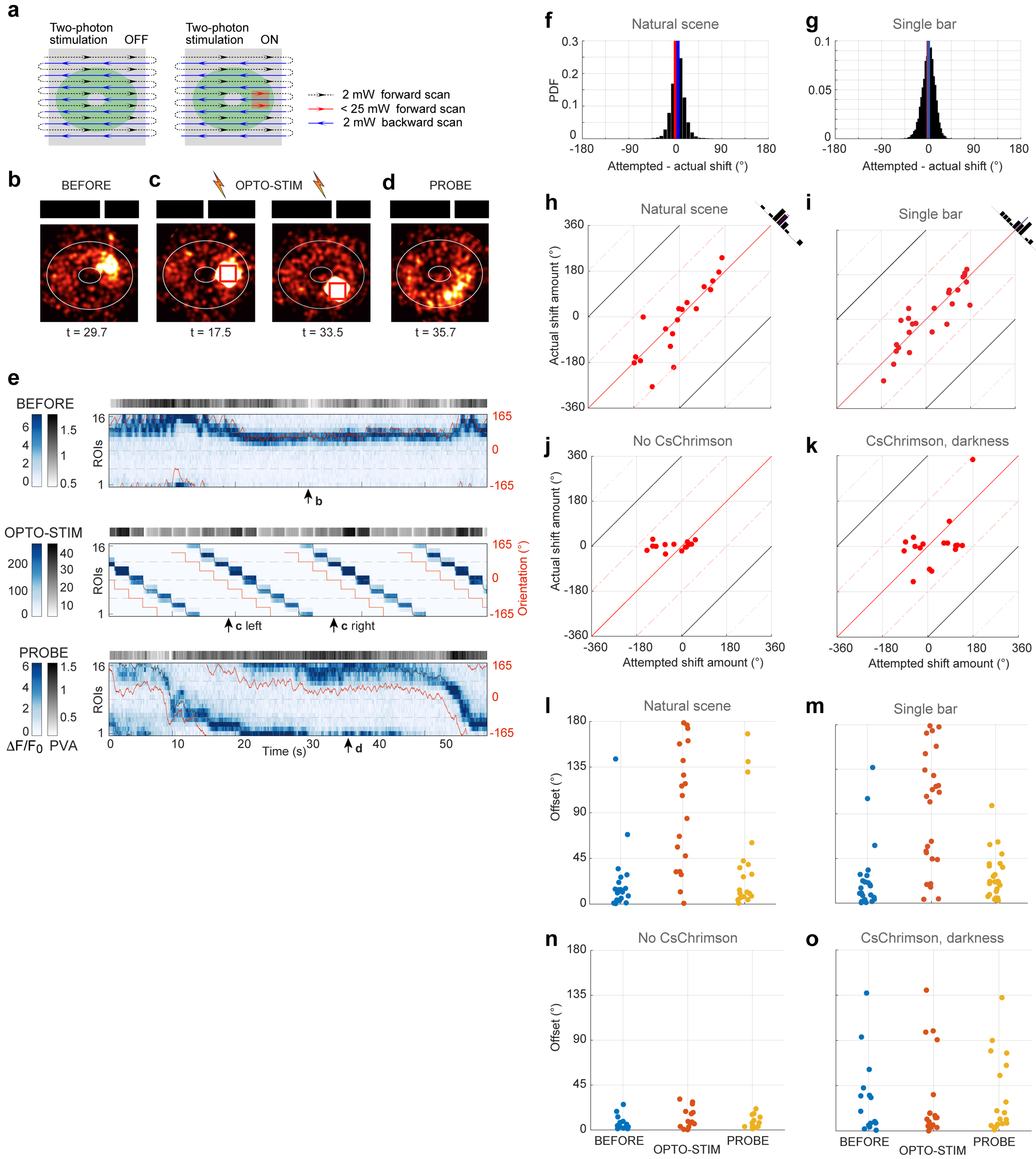

Extended Data Fig. 1 | See next page for caption.

Extended Data Fig. 1 | Manipulation of pinning offset of heading representation relative to visual scene. **a**, Schematic shows simultaneous calcium imaging and localized optogenetic stimulation. **b**–**d**, Snapshots of compass-neuron population activity before, during and after optogenetic manipulation in open loop (orientations of imposed single-stripe visual scene are shown at the top). **b**, A bump offset of close to zero before optogenetic manipulation (arrow in **e** shows the time of this snapshot). **c**, Optogenetic imposition of the new offset. Left, when the vertical stripe is in front of the fly, the bump was imposed on the right side of the ellipsoid body (rectangle). Right, 45° rotated scene and bump with the same offset as shown on the left. This offset was sequentially imposed across eight positions of the visual scene and ellipsoid body for approximately 2 s per position for 5 min (**e** middle). **d**, Snapshot of compass-neuron calcium transients after manipulation (**e** bottom). The bump position relative to same visual scene as in **b** is now shifted by the offset imposed in **c**. **e**, Segments (60 s) of imaging before (top), during (middle) and after (bottom) a 5-min optogenetic manipulation. Conventions are the same as in Fig. 1. **f**, Bootstrapped distribution of the mean difference between the imposed and actual offset shifts in Fig. 2 (natural scene), which was not significantly different from 0 (19 trials from 10 flies, bootstrapped mean difference test, two-sided, $P = 0.6276$). **g**, Bootstrapped distribution of the mean difference between the imposed and actual offset shifts in **b**–**d** (single stripe), which was not significantly different from 0 (25 trials from 14 flies, two-sided, $P = 0.8932$). **h**–**k**, Distribution of imposed (x axis) versus actual (y axis) offset shifts across flies. The distribution is significantly linear along the identity line (circular linearity test. **h**, Natural scene, 19 trials from 10 flies, $P < 0.0001$. **i**, Single stripe, 25 trials from 14 flies, $P < 0.0001$. **j**, No CsChrimson, 14 trials from 10 flies, $P = 0.0934$. **k**, In darkness, 17 trials from 10 flies, $P = 0.6064$). **l**–**o**, Absolute change in offset across two trials before manipulation (blue) and across two trials after manipulation (yellow), and absolute change in offset induced by manipulation (red). Bootstrapped mean difference tests, one-sided. n values are the same as in **h**–**k**. **l**, Natural scene, bootstrapped mean difference test between epochs before and during manipulation, $P = 0.0464$; and between epochs during and after manipulation, $P = 0.0024$. **m**, Single stripe, bootstrap tests of the mean difference showed a significant difference between the baseline offset shifts and manipulated offset shifts ($P = 0.0207$ between epochs before and during manipulation; and $P = 0.0252$ between epochs during and after manipulation). **n**, No CsChrimson control, bootstrap tests of the mean difference did not show any significant difference; $P > 0.05$ for all pairs. **o**, Darkness control, bootstrap tests of the mean difference did not show any significant difference; $P > 0.05$ for all pairs. Baseline offset shifts were comparable to the experimental group (**m**), but greater than the control group without CsChrimson (**n**). This suggests that the baseline offset variance in the experimental group might be due to a higher baseline activity of the compass-neuron population, induced by weak activation of CsChrimson during two-photon imaging.

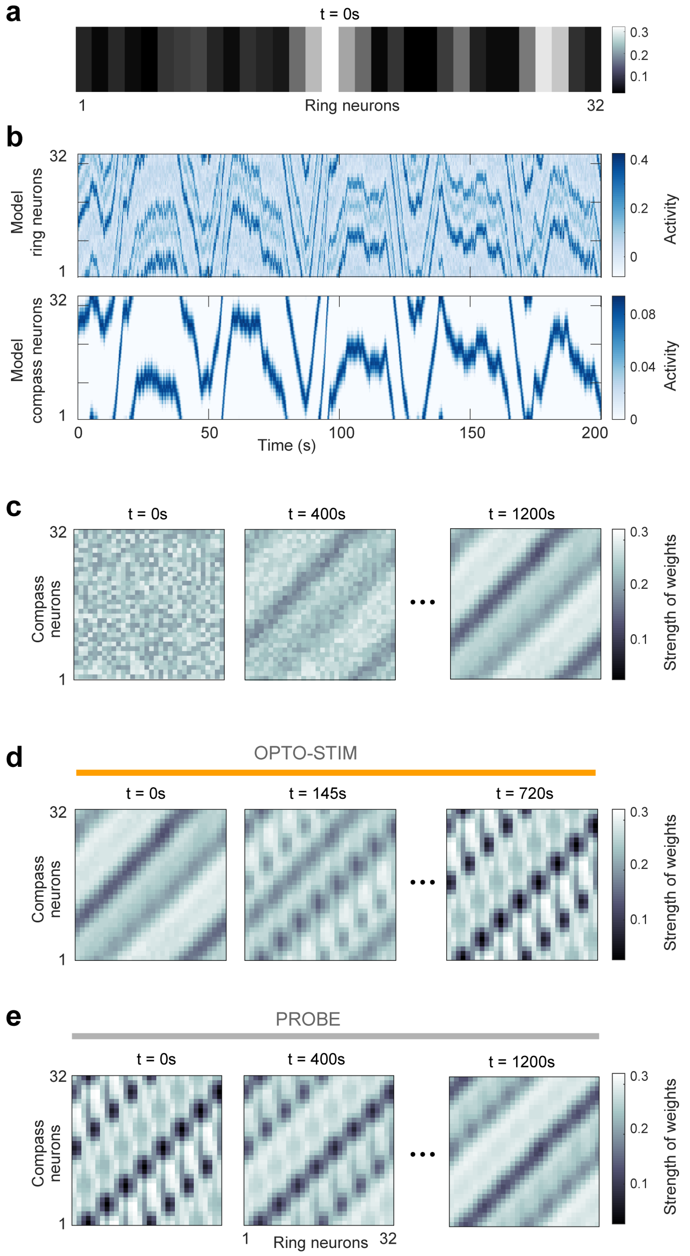

Extended Data Fig. 2 | Simulation showing the mapping of a complex scene onto a stable heading representation and optogenetic bump offset shifting. **a**, A complex one-dimensional scene was generated via a mixture of four von Mises functions with random mean directions and random concentration parameters, shown for $t = 0$. **b**, **c**, Model simulation. Ring-neuron population activity (**b**, top) serves as the assumed source of visual input. A time series of angular velocity obtained from tethered flight data was used to compute movement of the visual scene. **b**, Bottom, compass-neuron population activity during simulated orientation. **c**, Time-varying synaptic weights between ring and compass neurons. The simulation began with random synaptic weights (left) and random initial activity of compass-neuron population. Ring attractor dynamics ensures a stable bump, albeit with a random offset. The initial turning of bump is not enforced by visual cues but by the angular velocity signal from tethered flight data. The same 400-s turning signal was repeated 3 times (Supplementary Information). Synaptic weights stabilize over time (**c**, right). After learning, a vertical cross-section of the stabilized synaptic weight matrix resembles the model ring-neuron activity profile shown in **a**. **d**, Simulation of optogenetic shift in offset. The simulation began with the stable mapping shown in **c**. **e**, During the probe trial, the newly mapped offset was consolidated. All simulation results shown are based on a post-synaptically gated plasticity rule, unless otherwise stated. Extended Data Figures 5, 6 and Supplementary Information provide the differences in predictions made by post- and pre-synaptically gated plasticity rules.

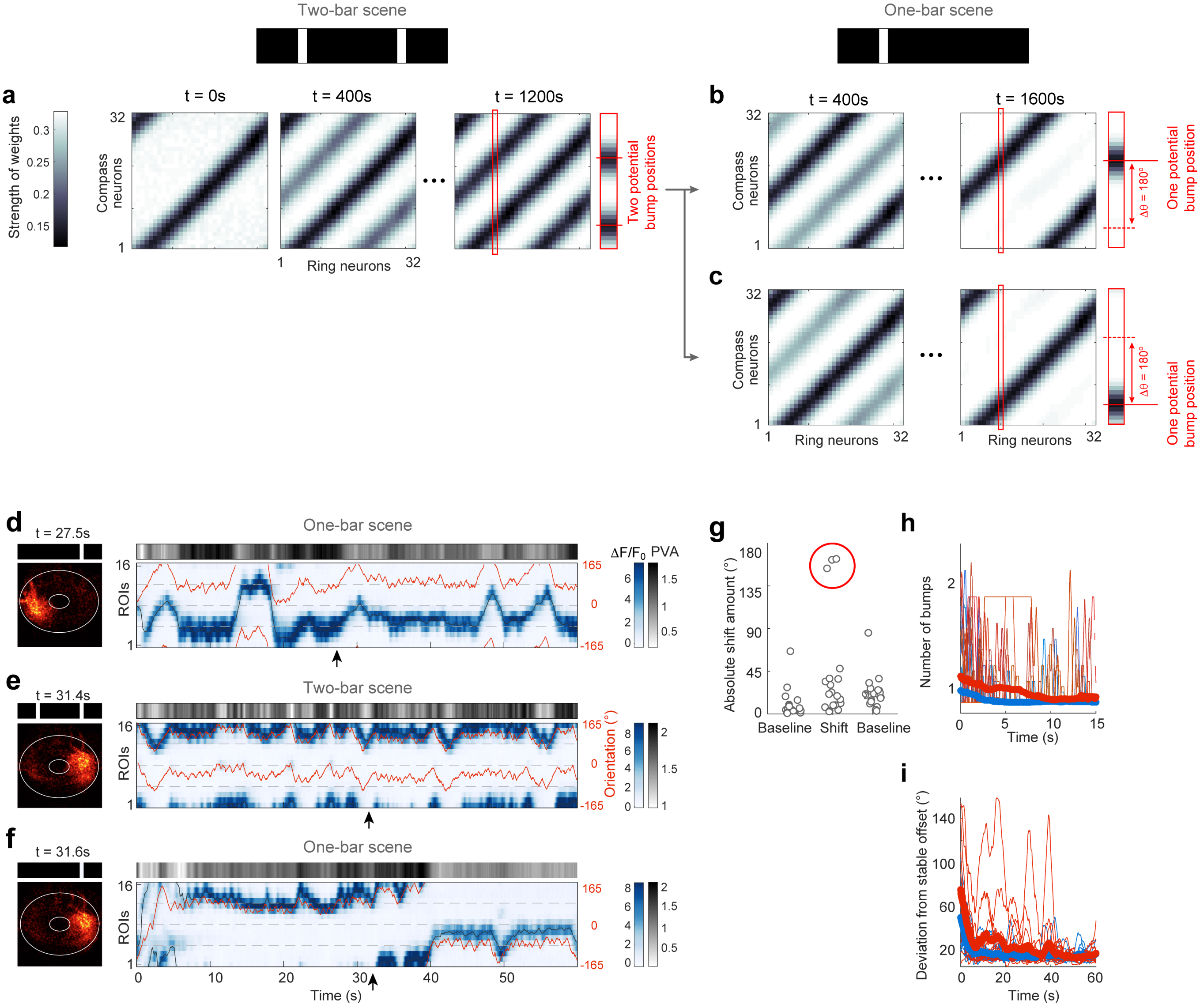

Extended Data Fig. 3 | Bump dynamics after a closed-loop two-stripe manipulation. a–**c**, Simulation of the time evolution of the synaptic weight matrix, induced by a visual scene with two vertical stripes. Conventions are the same as in Extended Data Fig. 2. **a**, The simulation began with the stabilized synaptic weight matrix shown in Fig. 2e. Visual input provided was two narrow von Mises functions, separated by 180°. Ring attractor dynamics ensured that the compass-neuron population maintained a single bump. Over time, the synaptic weight matrix develops two distinct bands of weak synapses (right), representing weakened connections from two active sets of ring neurons to a compass-neuron bump. **b**, **c**, When the system is then presented with a visual scene that has only one vertical stripe, there are two possible outcomes: ring attractor dynamics stabilizes an offset that is either shifted 180° from the original offset (**b**) or the same as the original offset (**c**). **d**–**i**, Natural bump-offset shifting with two identical vertical stripes (no optogenetic manipulation) separated by 165° in a 330° arena. **d**–**f**, Segments (60 s) of compass-neuron calcium transients before (**d**), during (**e**) and after (**f**) manipulation. Conventions are the same as in Fig. 2d, except that the red line represents the position of either one (**d**, **f**) or two (**e**) stripes. Imaging snapshots shown in the left panels were taken at times indicated with arrows beneath right panels. The bump offset is shifted by 180° in **f**, relative to its position in **e** (Supplementary Video 4). **g**, Distribution of the absolute shift in offset measured across trials from all flies. Left, baseline variance; change in offset across two trials before manipulation. Right, baseline variance; change in offset across two trials after manipulation. Centre, change in offset across two trials separated by a manipulation trial. In three cases ($n = 19$), the shift in offset was close to 180°. Unlike in simulations, in most two-stripe trials the bump position covers only half of the ellipsoid body because of the circular symmetry of the stimulus, which may underlie the apparently low yield of shifting (but see **h** and **i**; see Supplementary Information for further discussion). **h**, The number of bumps during the initial 15 s of 16 trials that did not exhibit a shift of 180° was significantly greater in trials that immediately followed a manipulation trial (red) than in a subsequent trial (blue) (bootstrap test of the mean difference, one-sided, $P = 0.0004$), indicating that initial competition between two bumps eventually stabilizes to a single bump. This implies that the manipulation trial generated two competing offsets. **i**, The deviation of the bump offset during the initial 15 s relative to the average bump offset during final 30 s of the same trial was also significantly greater in the trial immediately following a manipulation trial than in a subsequent trial (bootstrap test of mean difference, one-sided, $P = 0.0036$), which is a natural consequence of competition between two alternating bumps before one stabilizes.

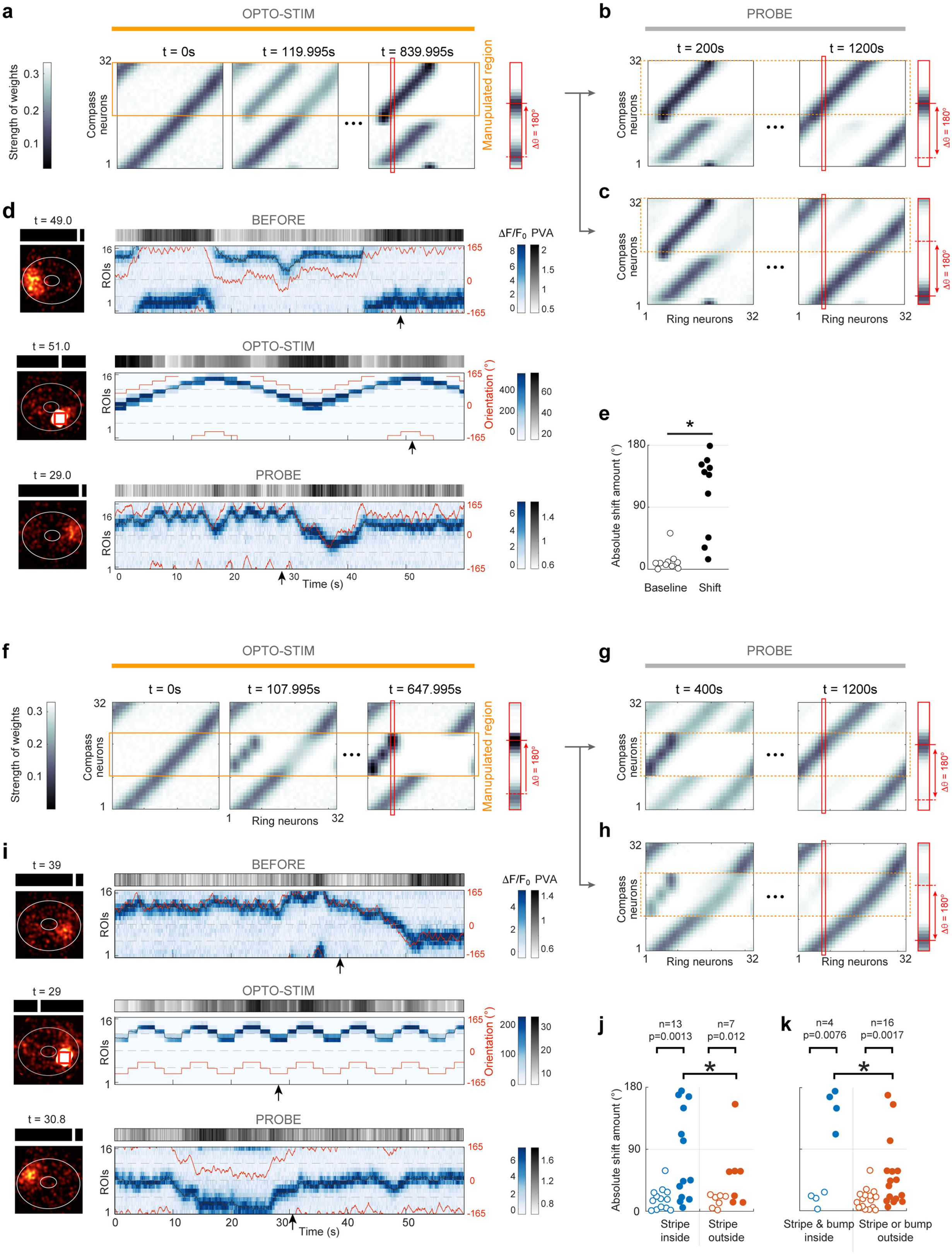

Extended Data Fig. 4 | See next page for caption.

Extended Data Fig. 4 | Global offset shift by local optogenetic manipulation. The conventions are the same as in Extended Data Fig. 2. **a**–**e**, Local optogenetic manipulation spanning 180°. **a**, The simulation begins with a stabilized synaptic weight matrix, shown in Fig. 2e. Over time, a new map spanning 180° replaced approximately half of the original map (right). A portion of the synaptic weight matrix, corresponding to visual orientations that were not presented, was erased over time (top right corner of right panel). **b**, **c**, After manipulation, two potential maps (the original map and the newly imposed map) compete. Which map it is that eventually stabilizes and strengthens depends on whether or not the bump and stimulus begin in the newly mapped region of the ellipsoid body in the trial that immediately follows manipulation. **d**, Compass-neuron calcium transients before (top), during (middle) and after (bottom) optogenetic manipulation spanning 180° of the visual scene and the ellipsoid body. The conventions are the same as in Fig. 2d. Compare the offsets in the top and bottom panels. **e**, Distribution of the absolute shift in offset, measured across flies. White dots, baseline before manipulation; black dots, offset shift by manipulation (10 flies, bootstrapped mean difference test, one-sided, $*P < 0.0001$). **f**–**k**, Local optogenetic manipulation spanning 60°. **f**, The simulation begins with the stabilized synaptic weight matrix shown in Fig. 2e. Over time, the newly imposed map replaces a portion of original map, which spans more than 60° because of the non-zero width (118° tail to tail) of the bump (bottom right). **g**, **h**, After the manipulation, two potential maps (the original map and the newly imposed map) compete. After the epoch of manipulation, if the bump begins in the manipulated region (**g**), the new map is likely to dominate and eventually strengthen. **i**–**k**, Optogenetic manipulation spanning 60° of the visual scene and the ellipsoid body. **i**, Segments (60 s) of compass-neuron population activity before (top), during (middle) and after (bottom) manipulation. The position of stripe (bottom) is not in the manipulated domain, yet the bump is shifted to the optogenetically imposed offset (compare the offsets in the top and bottom panels). **j**, Left, data from 60°-span manipulation, after which a closed-loop probe trial begins with the stripe in the position that was sampled during manipulation. Open dots, baseline variance of the offset around mean, before manipulation. Solid blue dots, shift in offset induced by 60°-span manipulation. Across the population, the shift was significant (bootstrapped mean comparison, one-sided, $P < 0.0013$). Right, data from 60°-span manipulation, after which closed-loop probe trial begins with the stripe outside the set of positions sampled during manipulation. Open dots, baseline variance. Solid red dots, shift in offset induced by manipulation. The shift was only marginally significant across the population (bootstrapped mean comparison, one-sided, $P = 0.012$). The global extrapolation of local manipulation was facilitated when the stripe began in manipulated positions in the probe trial (binomial exact test, $*P = 0.0059$) (Methods). **k**, Same data as in **j** but re-categorized. Left, in probe trials, both the bump and stripe began in a position sampled during the manipulation (4 out of 20 flies). All 4 flies showed a greater-than-90° shift during probe trials. Right, all other conditions (16 out of 20 flies). In total, 3 out of 16 flies showed a greater-than-90° shift. The facilitation of global extrapolation when both the bump and stripe began in manipulated positions was significant (binomial exact test, $*P = 0.0012$) (Methods).

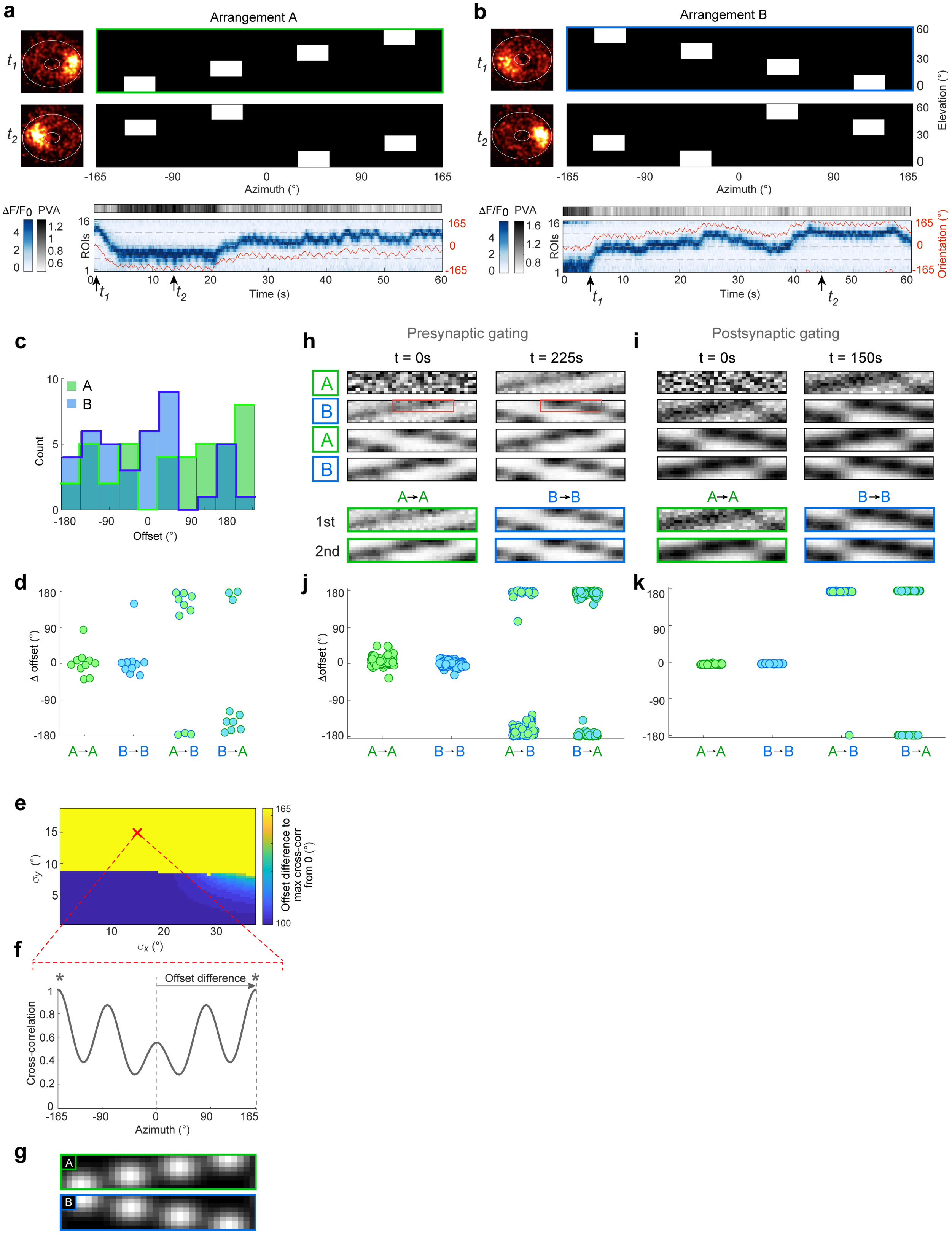

Extended Data Fig. 5 | See next page for caption.

Extended Data Fig. 5 | Deterministic offset difference between two artificial scenes with the same local feature but different two-dimensional organization. The Supplementary Information provides a detailed discussion. **a**, Compass-neuron calcium transients measured during closed-loop tethered flight in an artificial scene, arrangement A (A). The conventions are the same as in Fig. 1h. **b**, Calcium transients from the same fly as in **a**, but with a different artificial scene, arrangement B (B). **c**, Distribution of the mean offset of each trial, pooled across all flies (Methods). Distributions of offsets relative to scenes A and B were not significantly different from uniform ($n = 40$ trials from 10 flies, unimodality test by randomization, $P = 0.0819$ for A, $P = 0.1525$ for B). Compare with Fig. 1j. **d**, Distribution of offset shifts between two trials. The distribution of offset shifts between two artificial scenes, measured across flies, was significantly different from uniform distribution (unimodality test by randomization, from A to B, $n = 10$ flies, $P < 0.0001$; from B to A, $n = 10$ flies, $P < 0.0001$). The shift in offset was similar across different encounters with same scene, indicating that the offset was stable (unimodality test by randomization, from A to A, $n = 10$ flies, $P = 0.0001$; from B to B, $n = 10$ flies, $P = 0.0004$). Compare with Extended Data Fig. 6e. **e**, Parameter sweep to explore how two-dimensional Gaussian filters of different s.d., applied to the artificial scenes in **a** (arrangement A) and **b** (arrangement B), would affect shifts in offset between the two scenes. Filters represent the simplified effect of ring-neuron filtering of scenes. Shifts in offset should approximately match azimuthal shifts that would produce the best match (that is, maximum two-dimensional cross-correlation) between the filtered scenes. Each axis represents increasing s.d. of the applied two-dimensional Gaussian filter (**g**). The point marked with a red X is shown in **f**. **f**, Two-dimensional cross-correlation between two scenes in **a** and **b** after applying two-dimensional Gaussian filtering with 15° s.d. (red X in **e**). This filter size corresponds to a 30° full-width at half-maximum receptive field, which matches the average size of the minor axis of ellipses that fit ring-neuron receptive fields[13,39]. Higher filter sizes up to 60° full-width at half-maximum (the average size of the major axis of elliptical fits of ring-neuron receptive fields[13,39]) require similar azimuthal shifts to obtain a best match between the scenes (not shown in **e**). The azimuthal shift for the best match for this range of filters is 165°, a half rotation of the scene on the visual arena (as observed in **d**). **g**, Scenes in **a** and **b** after applying Gaussian filtering with 15° s.d. **h**, **i**, Simulation of pre- and post-synaptically gated plasticity rules applied when the model network is exposed to the two different filtered scenes shown in **g**. **h**, Evolution of the synaptic weight matrix with a pre-synaptically gated plasticity rule. Top left, initial random synaptic weight matrix from 8×32 ring neurons to 1 of 32 compass neurons. Top right, after exposure to scene A. Each compass neuron responds most to a snapshot of the scene at a particular orientation. Second row, after exposure to scene B, a new snapshot is mapped to the compass-neuron heading representation. The locations of the top two horizontal bars in arrangements A and B overlap (red rectangles), which corresponds to a 165° shift in the two-dimensional cross-correlation in **e** and **f** (or a 180° shift in the 360° arena in simulations). This deterministic offset shift results in the same pinning offset and a retrieval of the same heading representation as before when the scene is repeated later (bottom two rows). The third and fourth rows show repeated exposure to scenes A and B. Bottom two rows, retrieval of the original offset. **i**, Evolution of the synaptic weight matrix with post-synaptically gated plasticity rule. The result is almost identical to **h**, given that all ring neurons and compass neurons are activated during simulation. **j**, **k**, Simulated offset shifts with pre-synaptically (**j**) and post-synaptically (**k**) gated plasticity rules. For each rule, 100 simulations were performed. Both the pre-synaptic and the post-synaptic rules reproduced the population data in **d**.

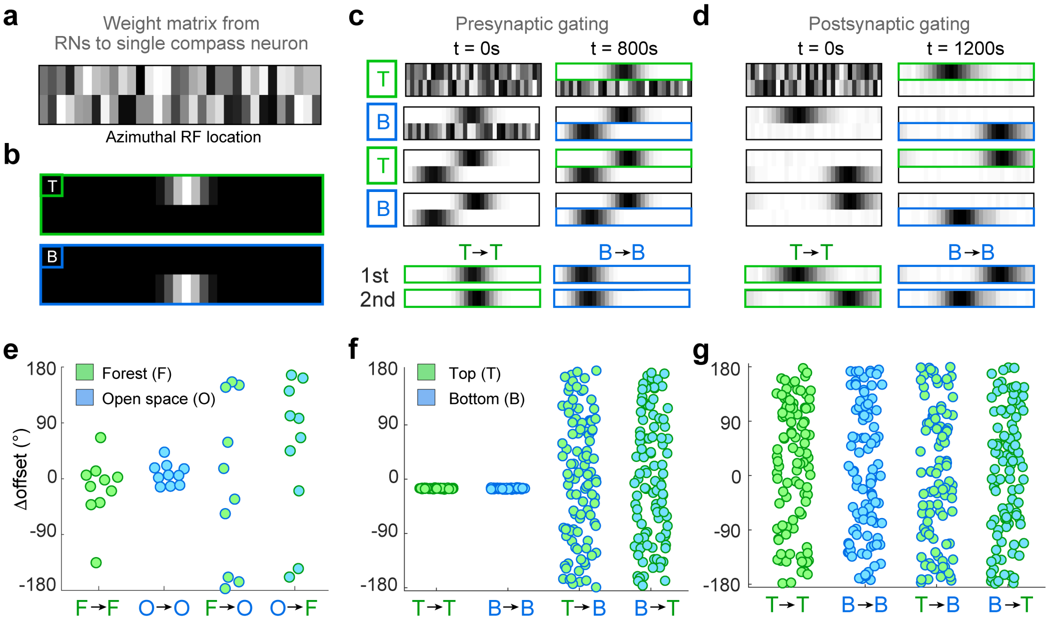

Extended Data Fig. 6 | Memory capacity of different plasticity rules. **a**–**d**, Simulation of pre- and post-synaptically gated plasticity rules with simple two-dimensional scenes. **a**, Initial random synaptic weight matrix from 2 × 32 ring neurons to 1 of 32 compass neurons. **b**, Two simple simulated scenes activate mutually exclusive ring neurons. T, top ring neurons are active; B, bottom ring neurons are active. **c**, Evolution of synaptic weights for a pre-synaptically gated plasticity rule. Top left, initial random weight matrix before presenting scene T. Top right, after exposure to scene T, only synapses from active ring neurons (top row of ring neurons in **e**) were updated, while synapses from all other ring neurons (bottom row of ring neurons in **e**) remained intact. Second row, after exposure to scene B, ring neurons that were previously inactive became activated, and their synapses were updated. Third row, when scene T was presented again, the offset between scene orientation and bump position was the same as when scene T was first presented (**f**). **d**, Evolution of synaptic weights for a post-synaptically gated plasticity rule. Synapses from inactive ring neurons are erased upon each encounter with a new scene. This would shift offset across two encounters of the same scene if the fly experiences a different scene between them. **e**, Population data are from ten flies. Distribution of offset shifts between two trials in Fig. 1h, i. The distribution of offset shifts between two different natural scenes, measured across flies, is not significantly different from uniform distribution (unimodality test by randomization, from F to O, $P = 0.489$; from O to F, $P = 0.1504$). Different encounters of the same scene lead to similar, near-zero offset shifts, indicating stability of offset (unimodality test by randomization, from F to F, $P = 0.0035$; from O to O, $P < 0.0001$). **f**, **g**, Simulated offset shifts with pre-synaptically (**f**) and post-synaptically (**g**) gated plasticity rules. For each rule, 100 simulations were performed.

nature research

Corresponding author(s): DBPR 2018-12-18453A
Last updated by author(s): Sep 18, 2019

Reporting Summary

Nature Research wishes to improve the reproducibility of the work that we publish. This form provides structure for consistency and transparency in reporting. For further information on Nature Research policies, see Authors & Referees and the Editorial Policy Checklist.

Statistics

For all statistical analyses, confirm that the following items are present in the figure legend, table legend, main text, or Methods section.

n/a	Confirmed	
☐	☒	The exact sample size (*n*) for each experimental group/condition, given as a discrete number and unit of measurement
☐	☒	A statement on whether measurements were taken from distinct samples or whether the same sample was measured repeatedly
☐	☒	The statistical test(s) used AND whether they are one- or two-sided *Only common tests should be described solely by name; describe more complex techniques in the Methods section.*
☐	☒	A description of all covariates tested
☐	☒	A description of any assumptions or corrections, such as tests of normality and adjustment for multiple comparisons
☐	☒	A full description of the statistical parameters including central tendency (e.g. means) or other basic estimates (e.g. regression coefficient) AND variation (e.g. standard deviation) or associated estimates of uncertainty (e.g. confidence intervals)
☒	☐	For null hypothesis testing, the test statistic (e.g. *F*, *t*, *r*) with confidence intervals, effect sizes, degrees of freedom and *P* value noted *Give P values as exact values whenever suitable.*
☒	☐	For Bayesian analysis, information on the choice of priors and Markov chain Monte Carlo settings
☒	☐	For hierarchical and complex designs, identification of the appropriate level for tests and full reporting of outcomes
☒	☐	Estimates of effect sizes (e.g. Cohen's *d*, Pearson's *r*), indicating how they were calculated

Our web collection on statistics for biologists contains articles on many of the points above.

Software and code

Policy information about availability of computer code

Data collection	Image collection (Scanimage 2016b), Behavioral image collection (StreamPix 6), Behavioral data collection (Matlab 2018b with NIDaq)
Data analysis	Data analyses (Matlab R2018b)

For manuscripts utilizing custom algorithms or software that are central to the research but not yet described in published literature, software must be made available to editors/reviewers. We strongly encourage code deposition in a community repository (e.g. GitHub). See the Nature Research guidelines for submitting code & software for further information.

Data

Policy information about availability of data

All manuscripts must include a data availability statement. This statement should provide the following information, where applicable:

- Accession codes, unique identifiers, or web links for publicly available datasets
- A list of figures that have associated raw data
- A description of any restrictions on data availability

All data and code are freely available without restriction at http://research.janelia.org/jayaraman/Kim_etal_Nature2019_Downloads/

Field-specific reporting

Please select the one below that is the best fit for your research. If you are not sure, read the appropriate sections before making your selection.

☒ Life sciences ☐ Behavioural & social sciences ☐ Ecological, evolutionary & environmental sciences

For a reference copy of the document with all sections, see nature.com/documents/nr-reporting-summary-flat.pdf

Life sciences study design

All studies must disclose on these points even when the disclosure is negative.

Sample size	The number of flies to collect was chosen to be 10, which is a sufficient number to perform non-parametric testings, for all experimental and control groups, unless mentioned otherwise in Methods.
Data exclusions	No exclusion of flies. In each fly, segments when fly was not flying were excluded from analyses.
Replication	The optogenetic bump offset shifting has been replicated ten times with different conditions, all of which reproduced significant effects. Five of them are reported in the manuscript.
Randomization	All flies in this study were randomly selected from their housing vials.
Blinding	Not applicable.

Reporting for specific materials, systems and methods

We require information from authors about some types of materials, experimental systems and methods used in many studies. Here, indicate whether each material, system or method listed is relevant to your study. If you are not sure if a list item applies to your research, read the appropriate section before selecting a response.

Materials & experimental systems

n/a	Involved in the study	
☒	☐	Antibodies
☒	☐	Eukaryotic cell lines
☒	☐	Palaeontology
☐	☒	Animals and other organisms
☒	☐	Human research participants
☒	☐	Clinical data

Methods

n/a	Involved in the study	
☒	☐	ChIP-seq
☒	☐	Flow cytometry
☒	☐	MRI-based neuroimaging

Animals and other organisms

Policy information about studies involving animals; ARRIVE guidelines recommended for reporting animal research

Laboratory animals	5- to 8-day old female Drosophila melanogaster
Wild animals	The study did not involve wild animals.
Field-collected samples	The study did not involve samples collected from the field.
Ethics oversight	No ethical approval or guidance was required for Drosophila physiological experiments.

Note that full information on the approval of the study protocol must also be provided in the manuscript.